Check for updates

Geochemistry, Geophysics, Geosystems®

AGU ADVANCING EARTH AND SPACE SCIENCES

RESEARCH ARTICLE
10.1029/2024GC011743

Magma Chamber Response to Ice Unloading: Applications to Volcanism in the West Antarctic Rift System

A. N. Coonin[1], C. Huber[1], J. Troch[2], M. Townsend[3], K. Scholz[4], and B. S. Singer[5]

[1]Department of Earth, Environmental, and Planetary Sciences, Brown University, Providence, RI, USA, [2]Division of Earth Sciences and Geography, RWTH Aachen University, Aachen, Germany, [3]Department of Earth and Environmental Sciences, Lehigh University, Bethlehem, PA, USA, [4]Department of Earth Sciences, University of Oregon, Eugene, OR, USA, [5]Department of Geoscience, University of Wisconsin-Madison, Madison, WI, USA

Key Points:

- During deglaciation, the evolution of a crustal magma chamber beneath kilometers of ice is sensitive to the rate at which ice is removed
- A critical rate of unloading can trigger additional eruption events
- Ice unloading expedites the onset of volatile exsolution, with consequences for magma chamber pressurization and eruption size

Supporting Information:

Supporting Information may be found in the online version of this article.

Correspondence to:

A. N. Coonin,
allie_coonin@brown.edu

Citation:

Coonin, A. N., Huber, C., Troch, J., Townsend, M., Scholz, K., & Singer, B. S. (2024). Magma chamber response to ice unloading: Applications to volcanism in the West Antarctic rift system. *Geochemistry, Geophysics, Geosystems*, *25*, e2024GC011743. https://doi.org/10.1029/2024GC011743

Received 2 JUL 2024
Accepted 26 OCT 2024

Abstract Volcanic activity has been shown to affect Earth's climate in a myriad of ways. One such example is that eruptions proximate to surface ice will promote ice melting. In turn, the crustal unloading associated with melting an ice sheet affects the internal dynamics of the underlying magma plumbing system. Geochronologic data from the Andes over the last two glacial cycles suggest that glaciation and volcanism may interact via a positive feedback loop. At present, accurate sea-level predictions hinge on our ability to forecast the stability of the West Antarctic Ice Sheet, and thus require consideration of two-way subglacial volcano-deglaciation processes. The West Antarctic Ice Sheet is particularly vulnerable to collapse, yet its position atop an active volcanic rift is seldom considered. Ice unloading deepens the zone of melting and alters the crustal stress field, impacting conditions for dike initiation, propagation, and arrest. However, the consequences for internal magma chamber dynamics and long-term eruption behavior remain elusive. Given that unloading-triggered volcanism in West Antarctica may contribute to the uncertainty of ice loss projections, we adapt a previously published thermomechanical magma chamber model and simulate a shrinking ice load through a prescribed lithostatic pressure decrease. We investigate the impacts of varying unloading scenarios on magma volatile partitioning and eruptive trajectory. Considering the removal of km-thick ice sheets, we demonstrate that the rate of unloading influences the cumulative mass erupted and consequently the heat released into the ice. These findings provide fundamental insights into the complex volcano-ice interactions in West Antarctica and other subglacial volcanic settings.

Plain Language Summary In regions like West Antarctica, volcanic eruptions occur underneath ice sheets. When hot magma comes in contact with ice, it can accelerate the melting of the ice cover. Beyond this, as climate change causes ice sheets to shrink, the decreasing weight on a volcano may affect its likelihood of erupting. The effects of ice loss above volcanoes on the underlying volcanic activity are not well understood. We conducted computer simulations to explore how gradual ice loss affects magma stored in the Earth's crust. We find that volcanoes beneath shrinking ice sheets are sensitive to the rate at which the ice sheet shrinks. As the ice melts away, the reduced weight on the volcano allows the magma to expand, applying pressure upon the surrounding rock that may facilitate eruptions. Additionally, the reduced weight from the melting ice above also allows dissolved water and carbon dioxide to form gas bubbles, which causes pressure to build up in the magma chamber and may eventually trigger an eruption. Under these conditions, we find that the removal of an ice sheet above a volcano results in more abundant and larger eruptions, which may potentially hasten the melting of overlying ice through complex feedback mechanisms.

1. Introduction

The ongoing stability of the West Antarctic Ice Sheet plays a crucial role in the prediction of modern sea-level rise. One of the Earth's largest reservoirs of land ice, the West Antarctic Ice Sheet is particularly vulnerable to collapse as it is largely grounded below sea-level (marine-based). As sea-level rises, such a marine-based ice sheet becomes increasingly submerged, accelerating the retreat of the grounding line (Gomez et al., 2020). Further, the bedrock underneath the ice sheet slopes downward from the current margins toward the interior of the ice sheet, promoting runaway retreat (Fretwell et al., 2013; Van Wyk de Vries et al., 2018). Factors affecting the stability of the West Antarctic Ice Sheet include atmospheric CO_2 emissions (e.g., Sutter et al., 2023), glacial isostatic adjustment and grounding line dynamics (e.g., Barletta et al., 2018; Gomez et al., 2015), ice shelf melting and calving due to interaction with a warming ocean (e.g., Stevens et al., 2020), and buttressing along the bedrock

© 2024 The Author(s). Geochemistry, Geophysics, Geosystems published by Wiley Periodicals LLC on behalf of American Geophysical Union.
This is an open access article under the terms of the Creative Commons Attribution-NonCommercial-NoDerivs License, which permits use and distribution in any medium, provided the original work is properly cited, the use is non-commercial and no modifications or adaptations are made.

15252027, 2024, 12, Downloaded from https://agupubs.onlinelibrary.wiley.com/doi/10.1029/2024GC011743 by Rwth Aachen University Universitätsbibliothek - 021000, Wiley Online Library on [18/12/2024]. See the Terms and Conditions (https://onlinelibrary.wiley.com/terms-and-conditions) on Wiley Online Library for rules of use; OA articles are governed by the applicable Creative Commons License

(e.g., Huybers et al., 2017; Pegler, 2018). While various studies investigate these parameters, one often overlooked factor is the potential for rapid ice loss to affect volcanic activity in the West Antarctic Rift System (WARS), which may promote further ice melting.

The West Antarctic Ice Sheet sits atop the WARS, a partially hidden complex network of active rifts comprising one of Earth's largest volcanic provinces. More than 100 eruptive centers are thought to be currently active, some exposed and some subglacial (LeMasurier et al., 1990; Smellie & Edwards, 2016; Van Wyk de Vries et al., 2018). While eruptions from kilometers-deep subglacial magmatic systems may not be directly observed, digital elevation models utilizing ice-penetrating radar indicate intact subglacial volcanic cones (Behrendt et al., 2002; Corr & Vaughan, 2008; Schroeder et al., 2014; Van Wyk de Vries et al., 2018). Given that rifting in West Antarctica initiated around 66 Ma and glaciation began around 34 Ma, the presence of intact subglacial cones today suggests ongoing volcanic and/or magmatic activity (Spiegel et al., 2016). Otherwise, basal friction with the ice sheet would have thoroughly eroded these structures (Van Wyk de Vries et al., 2018). Additionally, high regional heat fluxes (Schroeder et al., 2014; Shapiro & Ritzwoller, 2004), seismic activity (Lough et al., 2013), and geomagnetic anomalies (Blankenship et al., 1993) in West Antarctica suggest that the rift remains active to the present (Geyer et al., 2023).

The impacts of volcanic processes on the cryosphere and Earth's climate system, including decreased ice albedo (e.g., Bray, 1979; Möller et al., 2019) and outgassing of sulfur aerosols and CO_2 (e.g., Aubry et al., 2022; Handler, 1989; Huybers & Langmuir, 2009) have been investigated over a range of timescales. While it is widely understood that nearby magmatic and/or volcanic activity can accelerate ice melting, expansive geochronological records from the Andes provide strong evidence that changes in ice volume have influenced volcanic activity over the last deglaciation (Singer et al., 2024). However, little is known regarding the mechanisms by which a shrinking ice load at the surface affects magmatic systems at depth. Several solid Earth phenomena have been proposed to be triggered by deglaciation and to play into complex two-way processes: (a) changes in the crustal stress field, (b) deepening of the intersection of the adiabat and the solidus, and (c) a decrease in lithostatic pressure.

As the ice load above magma chamber retreats, the crustal stress field changes with time. These variations in stress conditions affect the likelihood that the magma chamber ruptures and transports magma through the crust. Flexure of the crust during isostatic rebound creates tensile stresses in the upper crust, promoting dike formation (Mora & Tassara, 2019; Wilson & Russell, 2020). This principle applies regardless of the nature of the load being removed; for example, Satow et al. (2021) suggested that a decrease in sea-level above the crust is capable of triggering dike injection from the Santorini magma chamber.

In addition, a shrinking ice load can increase the depth at which the geotherm crosses the solidus of mantle rock; as pressure from the overburden is reduced, the rock is enabled to melt deeper in the mantle, thereby extending the zone of decompression melting. The consequence of this augmented zone of melting is an increased melt flux to the magma chamber (Sigmundsson et al., 2010; Van Wyk de Vries et al., 2018). Jull and McKenzie (1996) modeled increased melt generation in response to the removal of an axisymmetric ice sheet above a mid-ocean ridge, with application to Iceland. Building on this work, Maclennan et al. (2002) examined this effect regarding volcanism in Iceland following the Last Glacial Maximum; they found that immediately after deglaciation, Icelandic eruption rates were 30–50 times higher than present-day levels and persisted for over 1,000 years post-deglaciation, owing to increased melt generation via decompression.

One intuitive consequence of unloading above a crustal magma chamber is the decrease in lithostatic pressure (pressure due to the weight of the overlying material), which affects the thermodynamic state and stability of magmatic phases at depth. Jellinek et al. (2004) developed a theoretical model illustrating that periodic glacial loading changes (mirroring glacial cycles) can affect the frequency of dike propagation from a magma chamber. As the magmatic overpressure exerts tensile stresses on the magma chamber walls, fractures can dilate, facilitating dike propagation (Jellinek & DePaolo, 2003). Further, Jellinek et al. (2004) argue that glacial loading changes may be especially influential with respect to the lithostatic stress conditions on shallow (5–8 km depth within the crust) magma chambers. However, the effect of such decreasing lithostatic pressure on internal magma chamber dynamics has yet to be investigated. While past studies have proposed a correlation between deglaciation and volcanic activity (Huybers & Langmuir, 2009; Rawson et al., 2016), the physical mechanisms linking dynamic ice loads and the evolution of underlying magmatic systems remain unclear. Consequently, assessments of the stability of the West Antarctic Ice Sheet and projections of its contribution to future sea-level rise lack potentially crucial information. Additionally, in West Antarctica, unloading-triggered volcanic activity could

15252027, 2024, 12, Downloaded from https://agupubs.onlinelibrary.wiley.com/doi/10.1029/2024GC011743 by Rwth Aachen University Universitätsbibliothek- 021000, Wiley Online Library on [18/12/2024]. See the Terms and Conditions (https://onlinelibrary.wiley.com/terms-and-conditions) on Wiley Online Library for rules of use; OA articles are governed by the applicable Creative Commons License

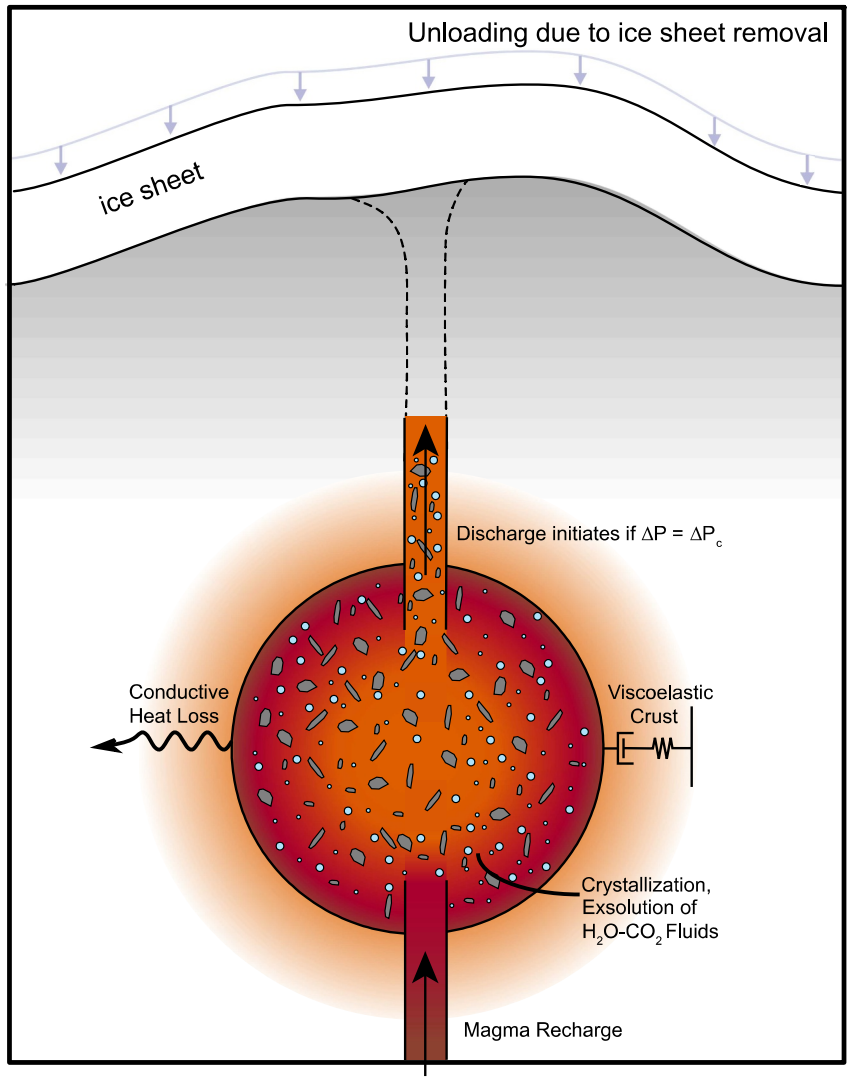


Figure 1. Schematic of the thermomechanical magma chamber model with simulated ice unloading from this study. Transparent arrows represent ice unloading as a decrease in the ice layer thickness over time.

pose additional hazards to future field campaigns. This highlights the need for physics-based modeling of subglacial magma chambers subjected to retreating ice loads to quantify the magmatic and/or volcanic effects of a time dependent removal of overburden pressure. To address this gap, we simulate the evolution of magma chambers with depth, size, composition, and volatile content in the range of those to be expected beneath the West Antarctic Ice Sheet, subject to cooling (leading to crystallization and exsolution), viscoelastic stress relaxation, magmatic recharge, and ice unloading (see Figure 1). Specifically, we test different rates of decreasing lithostatic pressure due to a shrinking surface load. Chen et al. (2006) estimate the rate of deglaciation-related surface unloading to be on the order of 10^{-5} Pa $\cdot$ s^{-1} in West Antarctica based on GRACE satellite data. We consider this a conservative estimate for the modern-day rate of ice unloading in West Antarctica, given the continuous increase in atmospheric CO_2 levels through to the present, and test rates of ice removal two orders of magnitude higher to represent accelerated ice loss in West Antarctica. Some ice streams of West Antarctica have experienced even higher rates of ice thinning, on the order of $10^{-0.5}$ Pa $\cdot$ s^{-1}, in the last decade (Hogg et al., 2021). For simplicity, we assume a linear lithostatic pressure drop over time for the removal of a finite surface load. We apply this forcing to a thermomechanical magma chamber model (Degruyter & Huber, 2014; Scholz et al., 2023) parametrized for West Antarctic basalt magmas with mixed CO_2 and H_2O contents to simulate and characterize the response of magma chamber evolution and eruption behavior to ice unloading. While we examine West

15252027, 2024, 12, Downloaded from https://agupubs.onlinelibrary.wiley.com/doi/10.1029/2024GC011743 by Rwth Aachen University Universitätsbibliothek- 021000, Wiley Online Library on [18/12/2024]. See the Terms and Conditions (https://onlinelibrary.wiley.com/terms-and-conditions) on Wiley Online Library for rules of use; OA articles are governed by the applicable Creative Commons License

Antarctic magmatic and/or volcanic activity here, our physical model of unloading can be extended to investigate the response of magma chambers (in other settings) to the removal of any uniform surface load, such as sudden reductions in sea-level over submarine volcanoes and erosion of overlying material during landslides or flank collapse.

2. Methods

To simulate WARS volcanoes, we employ a thermomechanical magma chamber model that includes water and carbon dioxide as magmatic volatile species (Degruyter & Huber, 2014; Scholz et al., 2023) tailored to West Antarctic Rift basalt compositions. Most exposed WARS deposits are part of the Marie Byrd Land (MBL) Province of West Antarctica (LeMasurier, 2013). To develop melting curves and H_2O-CO_2 solubility parametrizations specific to WARS basalts, we utilize whole rock compositions of basalts from MBL from the GEOROC database (https://georoc.eu/) to compute an average anhydrous magmatic composition (DIGIS Team, 2023). The major oxide contents of the average anhydrous WARS basalt composition used in this study and several parameters for the magma chamber model are provided in Table 1. Sample compositions and locations used to determine the average composition as well as their associated publications are provided in Table S1 of the Supporting Information S1.

We derive estimates for the range of initial H_2O and CO_2 contents from volatile compositions presented in Oppenheimer et al. (2011), Moussallam et al. (2014), and Lowenstern (2001). Combining these with our anhydrous WARS basalt composition, we simulate thermodynamic closed-system equilibrium crystallization using rhyolite-MELTS (Gualda et al., 2012). While rhyolite-MELTS v.1.1.0 is optimized for silicic systems, it is the only version of MELTS that accounts for both water and carbon dioxide at crustal pressures (Ghiorso & Gualda, 2015). After conducting multiple isobaric down-temperature crystallization runs at various pressures, we fit the outputs of the MELTS simulations via quadratic regression to develop mathematical expressions for (a) crystallinity and (b) CO_2 and H_2O solubilities as functions of temperature, pressure, and bulk volatile contents. We use a constant latent heat of melting computed as the median latent heat of melting over the entire temperature range from each MELTS simulation, averaged over all MELTS runs. Constant values for density, specific heat, and compressibility of the melt are computed as the median value of each respective parameter across the superliquidus portion of each individual MELTS simulation, averaged over all crystallization calculations. Similarly, for the crystal density and specific heat, we apply the same approach, instead using the portion of the MELTS simulation over which the magma is greater than 50% crystals by volume.

2.1. Melting Curves

We use 2184 isobaric crystallization simulations on rhyolite-MELTS v.1.1.0 with the average WARS basalt composition calculated from normalized anhydrous whole rock compositions over a range of fixed pressures and different initial CO_2 and H_2O conditions, as described in Table 1 (All MELTS calculations conducted at the oxygen fugacity of the NNO buffer.) From the raw MELTS outputs, we calculate volume fractions for melt, crystals/solids, and magmatic volatile phase (MVP). Employing the Matlab curve fitting application (cftool), we determine the most suitable function to describe the crystal volume fraction in the magma with respect to temperature.

Huber et al. (2009) postulated that the melt fraction (f) of magmas can be parametrized as a power law function with an exponent (b) describing the effect of magma composition:

$$f(T) = \left(\frac{T - T_{\mathrm{sol}}}{T_{\mathrm{liq}} - T_{\mathrm{sol}}}\right)^{b}, \qquad 0 < b < 1 \tag{1}$$

where T_{liq} is the liquidus temperature and T_{sol} is the solidus temperature. Considering mafic magmas, the power-law parametrization suggests an approximately linear melting curve with temperature ($b = 1$). Indeed, a linear fit for the melting curve (nominally the crystal volume fraction ϵ_x) as a function of temperature is satisfactory for MELTS simulations across a wide range of pressure, temperature, and volatile contents (Figure S1 in Supporting Information S1), with an accurate slope over the entire eruptible range (here taken to be $\epsilon_x < 0.5$; Caricchi et al., 2007; Marsh, 1981) and the liquidus temperature within 5% error of the MELTS data (see Figure S1 in Supporting Information S1).

15252027, 2024, 12, Downloaded from https://agupubs.onlinelibrary.wiley.com/doi/10.1029/2024GC011743 by Rwth Aachen University Universitätsbibliothek- 021000, Wiley Online Library on [18/12/2024]. See the Terms and Conditions (https://onlinelibrary.wiley.com/terms-and-conditions) on Wiley Online Library for rules of use; OA articles are governed by the applicable Creative Commons License

Table 1
Anhydrous Composition and Model Parameters for WARS Basalt

Major oxides for anhydrous WARS basalt composition											
	SiO_2	TiO_2	Al_2O_3	FeO_T	MnO	MgO	CaO	Na_2O	K_2O	P_2O_5	Total
wt. %	46.88	3.29	15.18	12.36	0.19	6.77	10.38	3.12	1.14	0.70	100.0

Parameters for WARS magma chamber model			
Symbol	Definition	Value	Units
c_m	Specific heat capacity of melt	1,142	J kg^{-1} K^{-1}
c_x	Specific heat capacity of crystals	1,160	J kg^{-1} K^{-1}
c_{CO_2}	Specific heat capacity of CO_2 fluid	1,200	J kg^{-1} K^{-1}
c_{H_2O}	Specific heat capacity of H_2O fluid	3,880	J kg^{-1} K^{-1}
M_{H_2O}	Molar mass of water	18.02×10^{-3}	kg mol^{-1}
M_{CO_2}	Molar mass of CO_2	44.01×10^{-3}	kg mol^{-1}
L_e	Latent heat of exsolution	610×10^3	J kg^{-1}
L_x	Latent heat of crystallization	470×10^3	J kg^{-1}
ΔP_c	Critical overpressure	20×10^6	Pa
α_r	Crustal thermal expansion coefficient	10^{-5}	K^{-1}
α_m	Melt thermal expansion coefficient	10^{-5}	K^{-1}
α_x	Crystal thermal expansion coefficient	10^{-5}	K^{-1}
β_m	Bulk modulus of melt	1.2×10^{10}	Pa
β_x	Bulk modulus of crystal	10^{10}	Pa
β_r	Bulk modulus of crust	10^{10}	Pa
κ	Thermal diffusivity of crust	10^{-6}	m^2 s^{-1}
ρ_m	Melt density	2,420	kg m^{-3}
ρ_x	Crystal density	2,900	kg m^{-3}
ρ_r	Density of crust	2,500	kg m^{-3}

Parameter space for rhyolite-MELTS simulations	
Pressure (MPa)	100–400 (intervals of 50 MPa)
wt. % H_2O	0.25–6 (intervals of 0.25 wt. %)
wt. % CO_2	0–1.1 (intervals of 0.1 wt. %)

Note. Anhydrous oxide abundances in wt. %, the parameter space covered by the rhyolite-MELTS v.1.1.0 simulations, and the derived parameters for the WARS magma chamber model.

We require a parametrization of the crystal volume fraction as a function of pressure and mass fractions of H_2O and CO_2 in the magma, in addition to temperature. As such, we perform a quadratic regression on the MELTS data to retrieve the following mathematical expressions for ε_x of WARS basalts as a function of temperature, pressure, and the total mass fractions of water and CO_2 in the magma chamber ($M^{tot}_{H_2O}$ and $M^{tot}_{CO_2}$, respectively):

$$\varepsilon_x\left(T, P, M^{tot}_{H_2O}, M^{tot}_{CO_2}\right) = A * T + B \quad (2)$$

where both A and B are functions of $P, M^{tot}_{H_2O}$, and $M^{tot}_{CO_2}$. The definitions of A and B as a function of $P, M^{tot}_{H_2O}, M^{tot}_{CO_2}$ obtained from the quadratic regressions are provided in Tables S2 and S3 of the Supporting Information S1.

2.2. Volatile Solubility

Following the procedure employed for ε_x, we reprocess the MELTS data for CO_2 and H_2O solubility in the magma. Isolating the simulations that reach volatile saturation while the magma is still eruptible ($\varepsilon_x < 0.5$), we use linear regression to fit the mass fraction of dissolved CO_2 and H_2O in the melt as a function of temperature,

pressure, and mole fraction of CO_2 in the magmatic volatile phase, X_{CO_2}. The resulting equation for dissolved H_2O in the melt is given by

$$M_{H_2O}^{diss} = c_1 + c_2T + c_3X_{CO_2} + c_4P + c_5(T * X_{CO_2}) + c_6(T * P) + c_7(X_{CO_2} * P) + c_8T^2 + c_9(X_{CO_2})^2 + c_{10}P^2 \quad (3)$$

with coefficients c_i listed in Table S4 of the Supporting Information S1.

While the parametrization for H_2O solubility obtained with this procedure is well-tuned to the MELTS data, the same approach could not be used to parametrize CO_2 solubility because of unrealistic spikes in CO_2 solubility within MELTS simulations when the first calcium-bearing phase clinopyroxene began to crystallize. These spikes likely reflect the increased activity of Ca^{2+}. In rhyolite-MELTS v.1.1.0, CO_2 dissolved in the melt is assumed to be exclusively present as carbonate species, leading to CO_2 activities co-varying with Ca activities. To refrain from fitting spurious CO_2 solubility values during the saturation of Ca-phases in MELTS, we instead employed the Liu et al. (2005) CO_2 solubility model for rhyolitic magmas. This model provides a good fit to the MELTS CO_2 solubility data outside the misleading spikes due to changes in Ca^{2+} activity. Liu et al. (2005) expresses the mass fraction of dissolved CO_2 (in ppm) by

$$M_{CO_2}^{diss} = \frac{(P * X_{CO_2})(5668 - 55.99P)(1 - X_{CO_2})}{(T + 273.15)} + P * X_{CO_2}\left(0.4133 * [P * (1 - X_{CO_2})]^{0.5}\right) + 2.041 \cdot 10^{-3} * [P * (1 - X_{CO_2})]^{1.5}. \quad (4)$$

Given that our target composition is basaltic, we tested the Liu parametrization extensively to check for consistency with the WARS basalt MELTS outputs (see Figures S2–S4 in Supporting Information S1). At the pressure-temperature conditions of interest to this study, the parametrizations agree well with the MELTS data (see Table 1 for valid range of conditions).

2.3. Magma Chamber Model

We apply our parametrization for WARS basalt crystallization and H_2O and CO_2 solubility to a thermo-mechanical magma chamber model adapted from Degruyter and Huber (2014) and Scholz et al. (2023). The magma chamber assumes a spherical body of eruptible magma (less than 50% crystals by volume), surrounded by a viscoelastic shell at depth in the crust, with the magma comprised of a mixture of melt, crystals, and dissolved or exsolved volatiles. We assume the magma is well-mixed with respect to phase and temperature. This assumption may ultimately underestimate the eruptible lifetime of a magma chamber. Over shorter timescales, the host crust deforms elastically to counteract volume-related pressure changes, while over longer timescales the surrounding crust accommodates overpressure by way of viscous relaxation. Heat loss from the magma chamber occurs through conduction to the surrounding crust, promoting crystallization of melt in the magma chamber and exsolution of H_2O and CO_2 as MVPs. Magma is injected into the system at a specified recharge rate, introducing heat to and pressurizing the chamber. The magmatic overpressure, ΔP, is defined as the difference between the pressure in the chamber and the lithostatic pressure exerted on the chamber. If a critical overpressure ΔP_c is achieved, the chamber will rupture and initiate a dike. We do not consider changes in the deviatoric stresses within the crust as the lithostatic pressure varies; thus, we use a constant critical overpressure of 20 MPa (in line with estimates from Rubin (1995)). Hence, our magma chamber model is appropriate for ice sheets with length scales much larger than the depth of the magma chamber (Singer et al., 2024). For simplicity in our model, we refer to this process of magma chamber rupture and dike initiation as an eruption. We do not directly consider whether the mass evacuated from the magma chamber will reach the Earth's surface (Taisne et al., 2011). This matter deserves attention in a future study where the stress field around the chamber is calculated. We simulate magma chamber evolutions with initial volumes (0.5 and 10 km^3) which are within the range of critical magma chamber sizes (~0.01–10 km^3) that must be exceeded for dikes to reach the surface based on coupled dike-magma chamber modeling (Townsend & Huber, 2020). This critical chamber size depends on the magma chamber depth, volatile content, and the critical overpressure. Although some modeled magma chambers may fail to surpass the threshold for eruptions initially, the magma chambers grow with time as they are fed by magmatic injection and can ultimately exceed the critical size for eruptions. During model eruptions, the mass outflow rate is set to 10^4 $kg \cdot s^{-1}$ (consistent with estimates from Mason et al. (2004)), until pressure returns to lithostatic and mass outflow ceases. In times of repose between eruptions, there is no mass outflow.

15252027, 2024, 12, Downloaded from https://agupubs.onlinelibrary.wiley.com/doi/10.1029/2024GC011743 by Rwth Aachen University Universitätsbibliothek, 021000, Wiley Online Library on [18/12/2024]. See the Terms and Conditions (https://onlinelibrary.wiley.com/terms-and-conditions) on Wiley Online Library for rules of use; OA articles are governed by the applicable Creative Commons License

15252027, 2024, 12, Downloaded from https://agupubs.onlinelibrary.wiley.com/doi/10.1029/2024GC011743 by Rwth Aachen University Universitätsbibliothek - 021000, Wiley Online Library on [18/12/2024]. See the Terms and Conditions (https://onlinelibrary.wiley.com/terms-and-conditions) on Wiley Online Library for rules of use; OA articles are governed by the applicable Creative Commons License

Without any unloading, the processes of magmatic injection, cooling, and viscous relaxation compete to control the magma chamber evolution. Degruyter and Huber (2014) define characteristic timescales for these processes to quantify the prevailing factors that govern a particular behavior of magma chamber evolution.

The timescale of magmatic injection is given by the ratio of the initial mass of the chamber to the magmatic recharge rate:

$$\tau_{\text{in}} = \frac{\rho_0 V_0}{\dot{M}_{\text{in}}} \tag{5}$$

The timescale of cooling is defined as follows:

$$\tau_{\text{cool}} = \frac{V_0^{2/3}}{\text{K}} \tag{6}$$

where K is the thermal diffusivity of the crust in $m^2\ s^{-1}$.

And lastly, the viscous relaxation timescale is given by

$$\tau_{\text{relax}} = \frac{\eta_{r_0}}{\Delta P_c}. \tag{7}$$

where τ_{relax} represents the time delay over which the crust surrounding a magma chamber can, via viscous creep, dissipate a pressure increase equal to that of the critical overpressure required to erupt, ΔP_c. If an overpressure greater than ΔP_c is generated over an interval of time shorter than τ_{relax}, the surrounding crust will respond elastically, unable to dissipate the overpressure, leading to eruptions. As in Degruyter and Huber (2014), the effective viscosity of the crust is a function of the crustal rheology and the temperature distribution around the chamber, which evolves with time. We introduce an additional timescale, τ_{ice} for the rate of lithostatic pressure reduction due to thinning ice at the surface (ice unloading rate), which is described in greater detail in the following section. The governing equations for the conservation of total mass, CO_2 and H_2O mass, and enthalpy within the magma chamber model follow the derivations from Scholz et al. (2023), with the WARS basalt parametrizations provided in Tables S2–S4 of the Supporting Information S1.

2.4. Pressure Unloading From Ice Removal at the Surface

To model ice unloading over a magmatic system, we decompose the primary variable governing magma chamber pressure in the Scholz et al. (2023) model into the sum of the lithostatic pressure (P_{lit}) and the magmatic overpressure (ΔP):

$$P = P_{\text{lit}} + \Delta P. \tag{8}$$

Differentiating with respect to time we have:

$$\frac{dP}{dt} = \frac{dP_{\text{lit}}}{dt} + \frac{d\Delta P}{dt}. \tag{9}$$

Without unloading, the lithostatic pressure remains constant over time, and thus the change in absolute pressure in the chamber is equal to the rate of change in magmatic overpressure. All magma chamber model simulations begin with an initial pressure equal to lithostatic and $\Delta P = 0$, hence, $P = P_{\text{lit}}$ at the onset. To investigate various scenarios of magma chamber evolution across a wide range of initial conditions, we consider different linear rates of lithostatic pressure decrease acting upon a wide range of potential WARS magma chambers (see Table 2). A constant unloading rate is imposed at the onset of the simulation. To prevent unrealistic lithostatic pressure drops (i.e., unloading after the ice is completely removed), we prescribe a maximum lithostatic pressure drop ($\Delta P_{\text{lit,max}}$) which is set to the pressure associated with removing the entire ice sheet. We run additional simulations of unloading associated with the removal of 1.5 and 2 km thick ice sheets with the same fixed rates of lithostatic pressure decrease for comparison (see Section 3.1).

15252027, 2024, 12, Downloaded from https://agupubs.onlinelibrary.wiley.com/doi/10.1029/2024GC011743 by Rwth Aachen University Universitätsbibliothek- 021000, Wiley Online Library on [18/12/2024]. See the Terms and Conditions (https://onlinelibrary.wiley.com/terms-and-conditions) on Wiley Online Library for rules of use; OA articles are governed by the applicable Creative Commons License

Table 2
Thermomechanical Magma Chamber Model Simulations

Model inputs	
Initial Volume (km^3)	0.5–10 km^3 in intervals of ~1 km^3
Depth (km)	6–10 km in intervals of 2 km
Magma Recharge Rate ($kg \cdot s^{-1}$)	10–100 $kg \cdot s^{-1}$ in intervals of ~5 $kg \cdot s^{-1}$
Initial wt. % H_2O	1–2 wt. % in intervals of 0.5 wt. %
Initial wt. % CO_2	0.05–0.5 wt. % in intervals of ~0.025 wt. %
Rate of Unloading (m/yr)	0 m/yr
	0.03 m/yr
	0.3 m/yr
	3 m/yr
Rate versus timescale of unloading:	
Rate of unloading ($Pa \cdot s^{-1}$)	Time required to remove 1-km ice sheet (years)
10^{-5}	30,000
10^{-4}	3,000
10^{-3}	300

We define the ice thinning timescale (τ_{ice}) mentioned above as the duration for removing an ice sheet of specified thickness from atop the magma chamber, given a specific rate of unloading ($\frac{dP_{lit}}{dt}$):

$$\tau_{ice} = \left| \Delta P_{lit,max} \left(\frac{dP_{lit}}{dt} \right)^{-1} \right|. \quad (10)$$

If the magma is still eruptible beyond τ_{ice} ($\varepsilon_x < 0.5$), the lithostatic pressure remains constant at $P_{lit}(t = 0) - |\Delta P_{lit,max}|$ for the remainder of the simulation. Regardless of whether the chamber is erupting or in repose, we solve for pressure, temperature, MVP volume fraction and CO_2 mole fraction in the MVP, from which all other quantities of interest including crystal volume fraction can be computed. Although this model is simple, its capacity to simulate nonlinear behavior enables the mapping of the magma chamber response to unloading-induced perturbations across an extensive parameter space. We generate an ensemble of 3,888 simulations from our parametrized magma chamber evolution model, exploring various initial magma chamber volumes, depths within the crust, magmatic recharge rates (upper limits from Gelman et al. (2013) and Annen (2009)), initial H_2O and CO_2 contents (Lowenstern, 2001; Moussallam et al., 2014; Oppenheimer et al., 2011), and rates of lithostatic pressure unloading (Chen et al., 2006; Hogg et al., 2021; see Table 2). The ice unloading rates considered in this paper include 0.03 m/yr $\left(10^{-5}\ Pa \cdot s^{-1}\right)$, 0.3 m/yr $\left(10^{-4}\ Pa \cdot s^{-1}\right)$, and 3 m/yr $\left(10^{-3}\ Pa \cdot s^{-1}\right)$, wherein a finite ice thickness is removed (e.g., 1 km).

3. Results

3.1. A Critical Rate of Ice Unloading

Ice unloading begins to dramatically affect magma chamber behavior when the rate of ice unloading approaches that of the other processes impacting magma chamber evolution (i.e., magmatic recharge, cooling, and viscous relaxation). At such conditions, the reduced confining pressure associated with unloading allows the magma to expand volumetrically generating overpressure. This source of overpressure associated with unloading acts in opposition to the prescribed lithostatic pressure decrease. As described in Section 2.3, within the model, an eruption (defined as any mass evacuation from the magma chamber) occurs when the difference between the magma chamber pressure and the lithostatic pressure at a given time exceeds the critical overpressure, ΔP_c. As lithostatic pressure decreases over time, the absolute pressure threshold required to reach ΔP_c is lowered. In some cases, this enables additional eruptions to occur solely due to unloading.

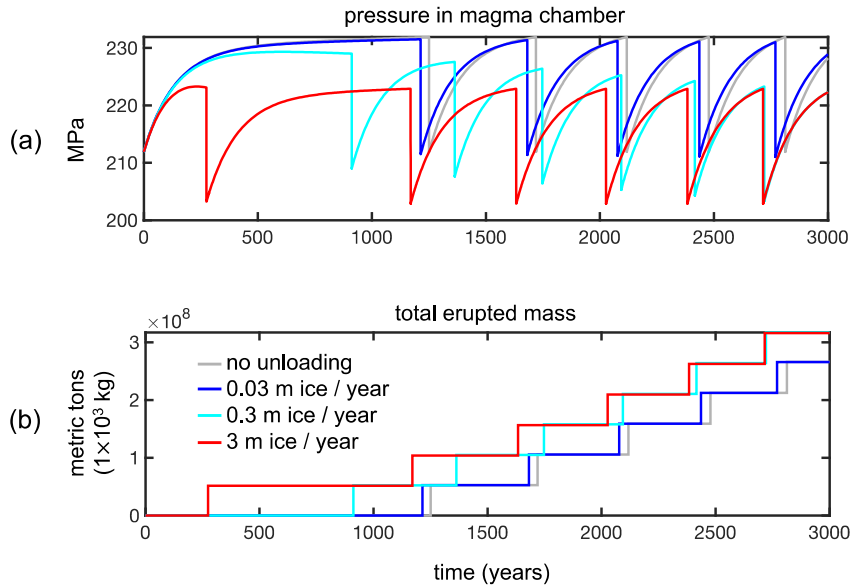


Figure 2. Increase in Total Erupted Mass with Unloading Rate: Volatile-Undersaturated. (a) Timeseries of pressure and (b) cumulative erupted mass over 3,000 years of magmatic evolution for an 8-km deep magma chamber initially with a volume of 5 km^3, 2 wt. % H_2O, and 500 ppm CO_2, subjected to a constant magmatic recharge rate of 20 $kg \cdot s^{-1}$. The chamber remains volatile-undersaturated during this time interval. Vertical drops in pressure correspond to eruption events. The slowest unloading scenario (blue; 0.03 m/year) plots closely over the zero-unloading case (gray). In the first 1,000 years, the slow unloading case is unable to reach the critical overpressure threshold; however, the overpressure generated through unloading causes the magma chamber to pressurize and erupt earlier than it would without unloading. In the first 1,000 years of the intermediate- (cyan; 0.3 m/year) and fast- unloading scenarios (red; 3 m/year), the combined overpressure from magmatic recharge and unloading surpasses the critical overpressure and triggers an additional eruption.

Figure 2 demonstrates one such situation, where a volatile-undersaturated magma chamber is pushed to erupt for an additional time when forced with a sufficient unloading rate. With the intermediate and high unloading rates (i.e., removing an ice sheet of 1 km thickness over approximately 3,000 and 300 years, respectively), the magma chamber reaches the critical overpressure earlier, producing an additional eruption that evacuates an additional 5×10^{10} kg. This additional erupted mass due to the ice unloading is an order of magnitude greater than, for example, the lava flows erupted from the summit of Mt Etna on 31 July 2021 (INGV, Rep. N 31/2021, ETNA, 2021). Such a rate-dependent increase in eruptions during the duration over which unloading is active also occurs in simulations of magma chambers at saturation conditions, despite the ability for the exsolved volatiles to buffer overpressure (see Figure S5 in Supporting Information S1).

We compare the sensitivity of the magma chamber response to both the rate of ice unloading and the total thickness of ice removed in Figure 3. While the integrated lithostatic pressure change is small in comparison to crustal pressures, a sufficient rate of unloading for a constant amount of ice removed (e.g., 1 km of ice load shaved off) can modulate the eruptive behavior. For both the lowest and intermediate unloading rates (blue and cyan, respectively) in Figure 3, the pressure trends are indistinguishable regardless of whether the ice removed is 1, 1.5, or 2 km thick. Only in the case of the highest unloading rate (red; Figures 3c and 3f) does the magnitude of ice removal cause subtle deviations.

For the smaller chamber in Figure 3 (panels a–c), the chamber cools efficiently ($\tau_{cool} = 1.4 \times 10^4$ years, $\tau_{in} = 1.6 \times 10^4$ years, $\tau_{relax} = 3.2 \times 10^4$ years), rheologically locking the magma via crystallization. Consequently, the total number of eruptions and erupted mass are identical regardless of the magnitude of the ice removed. There are eruptions from the magma chamber in Figures 3a–3c, but these are triggered by second boiling and hence occur even in the absence of unloading. A bigger magma chamber at the same depth, subjected to a higher rate of magmatic recharge (Figures 3d–3f), cools more slowly, maintaining the magma at less than 50% crystals by volume for longer. The magma chamber from Figures 3d–3f does not erupt without unloading; however, forcing with the intermediate unloading rate (0.3 m/yr) triggers several eruption events

15252027, 2024, 12, Downloaded from https://agupubs.onlinelibrary.wiley.com/doi/10.1029/2024GC011743 by Rwth Aachen University Universitätsbibliothek- 021000, Wiley Online Library on [18/12/2024]. See the Terms and Conditions (https://onlinelibrary.wiley.com/terms-and-conditions) on Wiley Online Library for rules of use; OA articles are governed by the applicable Creative Commons License

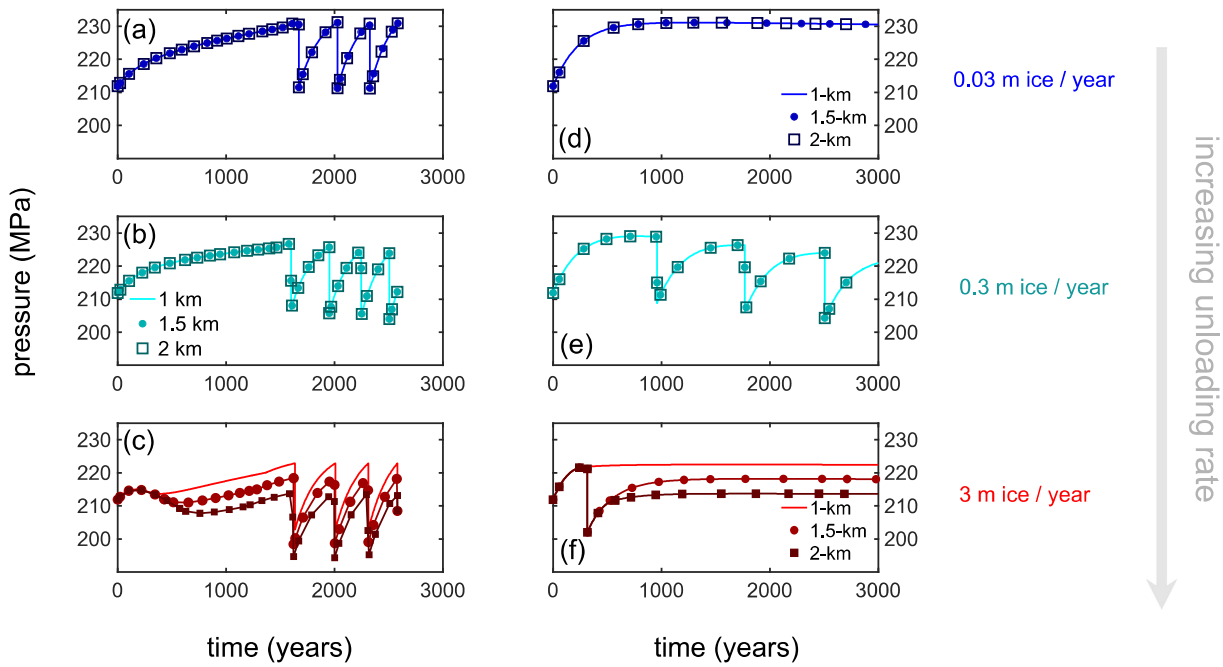


Figure 3. Unloading Rate versus Magnitude. (a–c) Pressure timeseries for an 8-km deep magma chamber with initial conditions of 1.25 km^3 volume, 2 wt. % H_2O, and 500 ppm CO_2, subjected to a constant magmatic recharge rate of 6 $kg \cdot s^{-1}$ and ice unloading rates of 0.03 m/year (a), 0.3 m/year (b), and 3 m/year (c). For a given rate of unloading in each panel, the pressure evolution is shown for three scenarios involving different magnitudes of unloading (1, 1.5, and 2 km of ice removal). (d–f) Pressure timeseries for an 8-km deep magma chamber with initial volume of 7 km^3 and volatile contents of 1 wt. % H_2O and 5,000 ppm CO_2, subjected to a constant magmatic recharge rate of 30 $kg \cdot s^{-1}$ and the same unloading rates.

(Figures 3e and 4). In the case of the highest unloading rate (0.03 m/yr; Figure 3f), a duration of unloading of 300 years is insufficient to counterbalance the dissipation of overpressure via viscous relaxation of the surrounding crust prior to complete removal of the ice load. If we consider the highest unloading rate again in Figure 3f, but increase the thickness of the ice removed, naturally, the magma "feels" the effects of decompression-induced volumetric expansion for longer. This, coupled with a slower cooling rate (compared to the magma chamber in Figures 3a–3c) and reduced pressure required to trigger an eruption enables a single eruption to occur. Figure 4 explores, in isolation, the 1 km ice removal scenarios for the magma chamber in Figures 3d–3f, demonstrating that even with the removal of modest amounts of ice (equivalent to less than 5%–10% of the lithostatic pressure exerted on a magma chamber at several kilometers deep in the crust), if the rate of ice unloading for a given ice load is sufficient, there are notable differences in eruptive behavior. From these observations, we conclude that the rate of unloading plays a greater role in controlling magma chamber evolution than the magnitude of unloading when considering the removal of km-thick ice loads. Hence, we primarily focus on the effects of unloading rates in Section 4.

3.2. Ice Unloading Expedites Exsolution of Magmatic Volatile Phase

Besides the potential for additional eruptions triggered by unloading-induced overpressure, unloading can also expedite or trigger the exsolution of volatiles from magmas on the cusp of volatile saturation. Partitioning of the CO_2 and H_2O between melt and fluid bubbles controls magma compressibility and thus the frequency and size of eruptions (Degruyter et al., 2017; Huppert & Woods, 2002; Townsend et al., 2019). All other factors being equal, we find that for magma chambers that are initially volatile-undersaturated, the time to the first exsolution of volatiles decreases by tens to hundreds of years as the rate of ice unloading increases (Figure 5; Figure S6 in Supporting Information S1). In Figure 5, while the variations in the total number of eruptions across various unloading rates are subtle, the cumulative mass erupted from the magma chamber is highly sensitive to the proportion of eruptions that occur after volatile exsolution due to increased magma compressibility. As illustrated in Figures 5b and 5c, the drop in lithostatic pressure also leads to a larger background exsolved fluid volume fraction. Even small increases in the exsolved fluid volume fraction enhance magma compressibility, augmenting the size of eruptions. The effects of unloading on magmatic volatile phases (and hence the total mass erupted from

15252027, 2024, 12, Downloaded from https://agupubs.onlinelibrary.wiley.com/doi/10.1029/2024GC011743 by Rwth Aachen University Universitätsbibliothek- 021000, Wiley Online Library on [18/12/2024]. See the Terms and Conditions (https://onlinelibrary.wiley.com/terms-and-conditions) on Wiley Online Library for rules of use; OA articles are governed by the applicable Creative Commons License

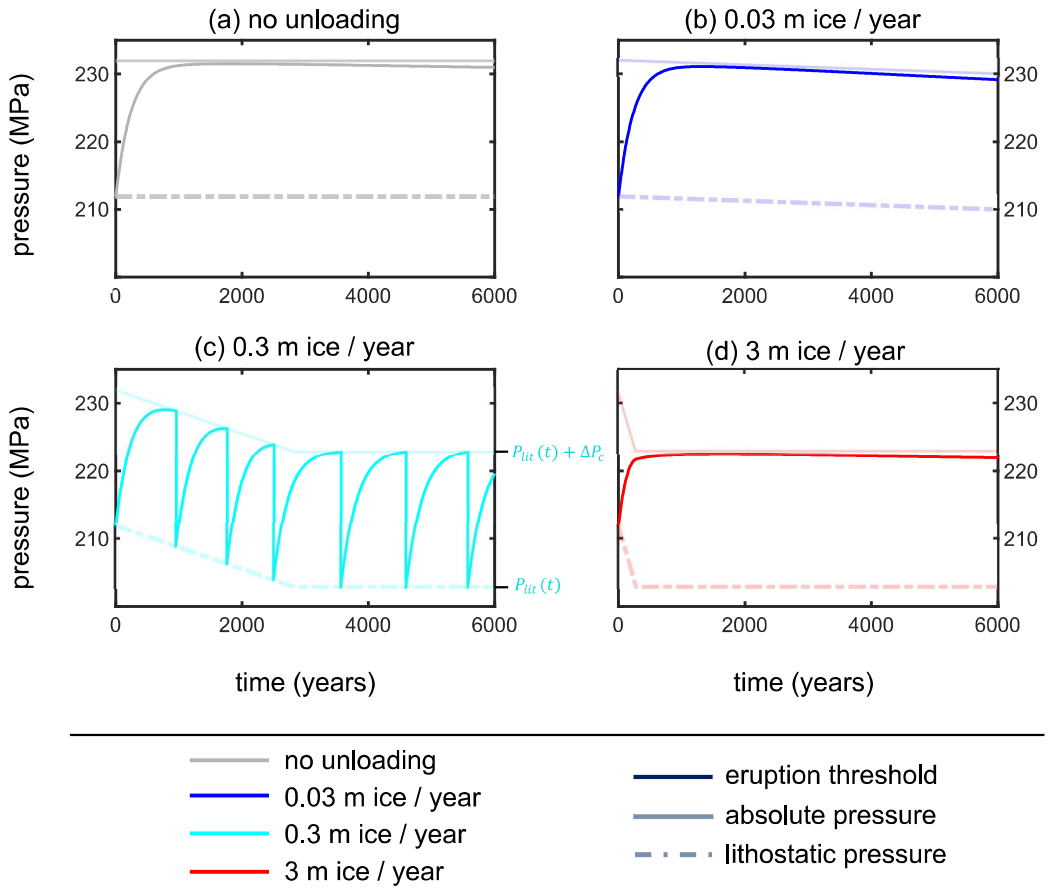


Figure 4. Pressure Budget for Eruption. Pressure timeseries for the same magma chamber in Figures 3d–3f subjected to (a) no ice unloading, and 1 km of ice removal at (b) low (0.03 m/yr), (c) intermediate (0.3 m/yr), and (d) high unloading (3 m/yr) rates, respectively. In (a), (b), and (d) the magma pressure falls just short of the critical overpressure required for eruptions. The highest unloading rate (d) experiences complete removal of the ice load early on, ceasing active unloading before the critical overpressure is reached. In the intermediate unloading scenario (c), the magma chamber erupts several times as unloading is active long enough for the lithostatic pressure to drop such that the overpressure reaches the requirement for eruptions.

the system) across the wider parameter space of potential WARS magma chambers are discussed further in Section 4.1.

4. Discussion

Sections 2.3 and 2.4 introduce representative timescales for the fundamental processes (cooling magmatic injection, viscoelastic relaxation of stresses by the surrounding crust, and ice unloading) competing to determine the evolution of a given magma chamber ($\tau_{cool}, \tau_{in}, \tau_{relax}$, and τ_{ice}, respectively). The ratio of these timescales offers a relative measure of the dominant processes. For instance, if the timescale for magma recharge is much smaller than the cooling and viscous relaxation timescales, magmatic recharge can counteract cooling and prolong the duration over which the magma is eruptible. In such a situation, overpressure cannot be efficiently dissipated by viscous creep in the surrounding crust. It is therefore useful to consider the ratios of $\tau_{cool}, \tau_{relax}$, and τ_{ice} and the timescale of magmatic injection, τ_{in}, to obtain the following dimensionless numbers, derived in Degruyter and Huber (2014):

$$\theta_1 = \frac{\tau_{cool}}{\tau_{in}}, \tag{11}$$

15252027, 2024, 12, Downloaded from https://agupubs.onlinelibrary.wiley.com/doi/10.1029/2024GC011743 by Rwth Aachen University Universitätsbibliothek- 021000, Wiley Online Library on [18/12/2024]. See the Terms and Conditions (https://onlinelibrary.wiley.com/terms-and-conditions) on Wiley Online Library for rules of use; OA articles are governed by the applicable Creative Commons License

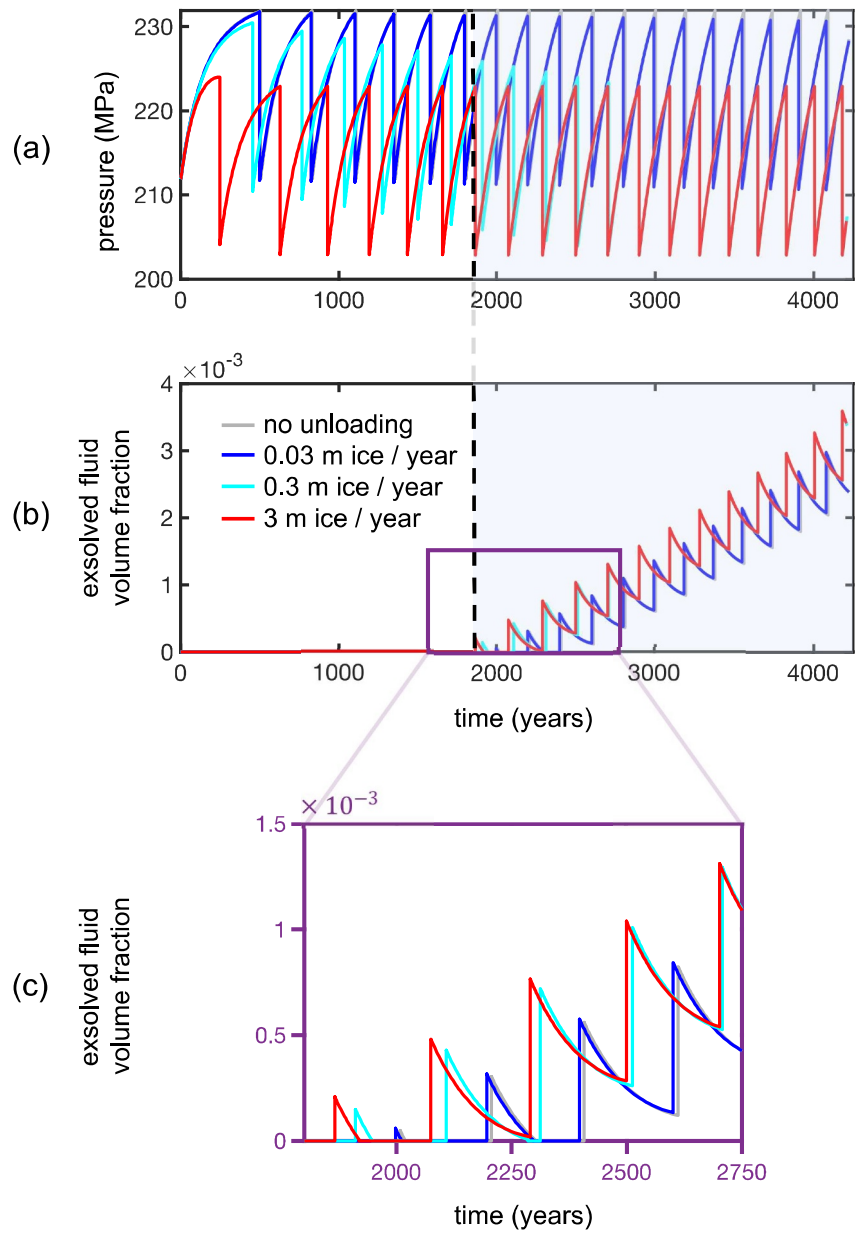


Figure 5. Expedited Onset of Volatile Exsolution. Pressure and exsolved fluid volume fraction timeseries for a magma chamber with a volume of 10 km^3 and 2 wt. % H_2O, and 500 ppm CO_2 initially, at depth of 8 km with a constant recharge rate of 12 $kg \cdot s^{-1}$. The magma chamber undergoes two oscillations of volatile saturation, as the pressure buildup toward eruption forces the volatiles to be redissolved in the melt. The pressure drop during an eruption releases the volatiles from the solution. As cooling proceeds, the magma chamber becomes for the remainder of the eruptible lifetime of the chamber.

$$\theta_2 = \frac{\tau_{\text{relax}}}{\tau_{\text{in}}}, \tag{12}$$

$$\theta_3 = \frac{\tau_{\text{ice}}}{\tau_{\text{in}}} \tag{13}$$

The timescale of ice unloading (Equation 10) is a function of the total magnitude of lithostatic pressure removed atop the system and the rate at which the lithostatic pressure decreases from ice unloading. Degruyter and Huber (2014) established a dimensionless eruption regime diagram using θ_1 and θ_2. We visualize our magma

15252027, 2024, 12, Downloaded from https://agupubs.onlinelibrary.wiley.com/doi/10.1029/2024GC011743 by Rwth Aachen University Universitätsbibliothek- 021000, Wiley Online Library on [18/12/2024]. See the Terms and Conditions (https://onlinelibrary.wiley.com/terms-and-conditions) on Wiley Online Library for rules of use; OA articles are governed by the applicable Creative Commons License

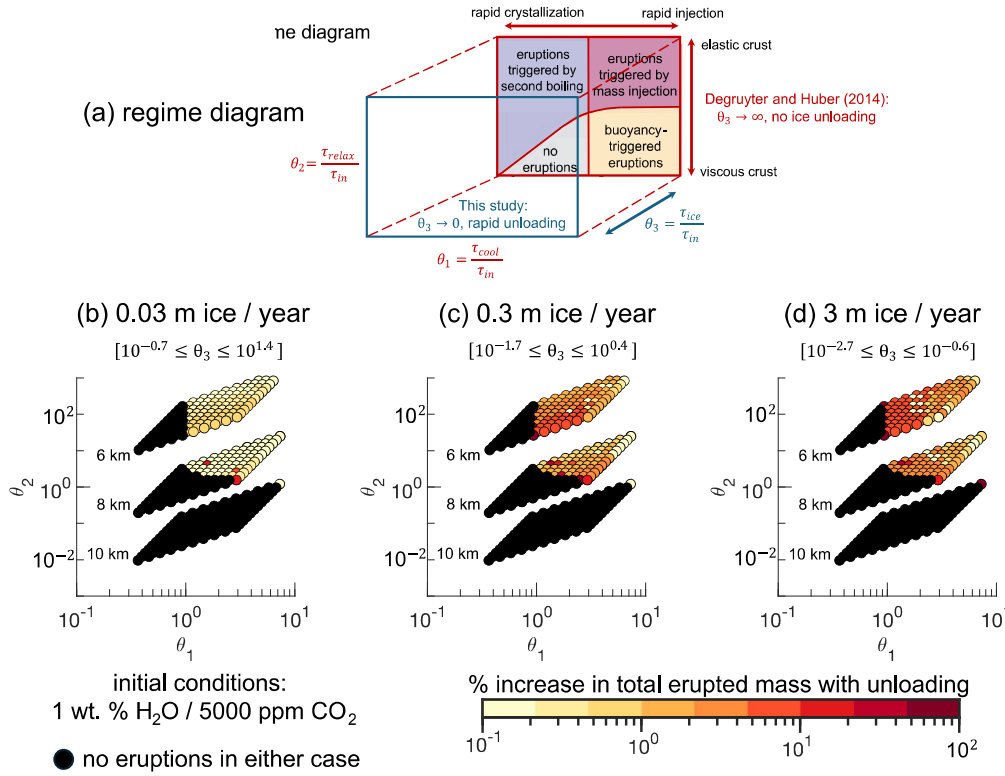


Figure 6. Increase in Mass Erupted with Unloading. (a) Modified regime diagram from Degruyter and Huber (2014). (b–d) Percent change in the total erupted mass between the zero-unloading case and unloading of 1 km of ice at 0.03 m/yr (b), 0.3 m/yr (c), and 3 m/yr (d), for magma chamber simulations with 1 wt. % H_2O and 5,000 ppm CO_2 initially. Black circles represent magma chambers that do not exist in either case (with or without unloading). Also provided are the range of θ_3 values corresponding within each panel. Since θ_3 is equal to the ratio of the ice unloading timescale to the magma injection timescale, even if the unloading rate is held constant, the values of θ_3 will vary across chambers with different initial volumes and magmatic recharge rates. For a particular timescale of magmatic injection, the value of θ_3 decreases with increasing ice unloading rate.

chamber parameter space as a 3D extension of their scaling relationships, with $\theta_1 = \frac{\tau_{cool}}{\tau_{in}}$ and $\theta_2 = \frac{\tau_{relax}}{\tau_{in}}$ on the x- and y- axes respectively and $\theta_3 = \frac{\tau_{ice}}{\tau_{inj}}$ plotted along the axis extending into and out of the plane of the page (Figure 6a). In the following subsections, we use this dimensionless 3D space to discuss the regimes of magma chambers most vulnerable to perturbations in cumulative erupted mass (and thus enthalpy released to the ice sheet). Subsequently, we place these findings in the context of post-Last Glacial Maximum trends in volcanism in the Andes and address future implications of the ice-volcanism feedback loop.

4.1. Unloading Effects on Total Erupted Mass

Within the context of the dimensionless timescale ratios (Equations 11–13), our results highlight the combinations of magma chamber conditions that are sensitive to unloading-induced perturbations in total erupted mass. Figures 6b–6d plot the percent increase in the total mass erupted with ice unloading compared to the equivalent magma chamber simulation without unloading. Unloading-induced perturbations in the total erupted mass from a magma chamber occur when both the cooling timescale and the viscous relaxation timescales are comparable or greater than the magma recharge timescale (θ_1, $\theta_2 > 1$). Within this range of magma chamber conditions, ice unloading raises the total erupted mass even at the most conservative unloading rate (0.03 m/yr). Deeper in the crust, the viscous relaxation of accumulated stresses inside the magma chamber by the surrounding crust dominates magma chamber evolution, reducing the ability for the magma chamber overpressure to exceed the eruption threshold. At shallower depths (larger values of θ_2), where magma chambers cool more rapidly and are generally more short-lived, there is a clear trend of increasing cumulative mass erupted with an increased unloading rate. In addition, the unloading effects can outcompete those of higher rates of magmatic injection, extending the region

15252027, 2024, 12, Downloaded from https://agupubs.onlinelibrary.wiley.com/doi/10.1029/2024GC011743 by Rwth Aachen University Universitätsbibliothek - 021000, Wiley Online Library on [18/12/2024]. See the Terms and Conditions (https://onlinelibrary.wiley.com/terms-and-conditions) on Wiley Online Library for rules of use; OA articles are governed by the applicable Creative Commons License

15252027, 2024, 12, Downloaded from https://agupubs.onlinelibrary.wiley.com/doi/10.1029/2024GC011743 by Rwth Aachen University Universitätsbibliothek, 021000, Wiley Online Library on [18/12/2024]. See the Terms and Conditions (https://onlinelibrary.wiley.com/terms-and-conditions) on Wiley Online Library for rules of use; OA articles are governed by the applicable Creative Commons License

of sensitivity to increases in erupted mass. Exceedingly rapid magmatic recharge will overprint the effects of unloading unless unloading occurs at a critical rate (i.e., the unloading timescale is less than or on the order of the magmatic injection timescale, $\theta_3 \leq 1$.)

As already described in Section 3.1, the unloading-related increase in the erupted mass illustrated in Figure 6 is in part driven by additional unloading-triggered eruption events. These eruptions are driven by two underlying mechanisms: first, overpressure is generated through the decompression-induced volumetric expansion of the magma. Second, unloading alters the pressure budget required for the magma chamber to erupt, and as the overburden pressure decreases, a lower absolute pressure in the magma chamber is required to exceed the overpressure criteria for eruptions (Equation 8; Figure 4). These combined effects result in eruptions that would not occur in the absence of unloading, leading to a greater cumulative mass erupted over the lifetime of the magma chamber. As demonstrated in Figure 3 and Figure S5 in Supporting Information S1, these additional unloading-triggered eruptions are observed from magma chambers that are volatile-undersaturated and oversaturated alike. For magma chambers initially below the threshold of volatile saturation, these eruptions tend to occur while the volatiles are completely dissolved in the melt, since the magma is less compressible without exsolved fluid bubbles (see Figure S9 in Supporting Information S1).

An additional source of the observed increase in cumulative erupted mass with unloading rate (Figure 6) is the quantity of larger-sized eruptions, resulting from increased magma compressibility, as decompression promotes the release of volatiles from the melt. In Section 3.2, we show that with sufficient unloading rates, magma chambers initially below saturation conditions begin to exsolve volatiles earlier due to decompression. A regime diagram demonstrating the extent of sensitivity of initially volatile-undersaturated magma chambers to an expedited transition to volatile saturation is provided in Figure S10 of the Supporting Information S1. Interestingly, the magma chambers that are most sensitive to earlier volatile saturation with unloading are cases that fail to erupt due to insufficient magmatic recharge (compare Figure 6 and Figure S10 in Supporting Information S1); these magma chambers are just short of the requirements to erupt but with slight perturbations in magmatic recharge could be pushed beyond the threshold. Magma chambers subjected to unloading will experience volatile saturation earlier in their evolution, resulting in the potential for more eruptions while the magma is volatile-saturated (and hence more large eruption events). Nevertheless, there is still modest sensitivity to an earlier onset of volatile saturation with sufficient rates of unloading for magma chambers that do erupt, resulting in a greater cumulative mass erupted even without a change in the total number of eruptions (Figure 7). Regardless of whether the chamber is initially volatile-saturated or becomes saturated later, with ice unloading (even if only active for a short duration with respect to the eruptible lifetime of the magma chamber), the volatile solubility is permanently reduced, resulting in increased magma compressibility and larger eruptions. Such long-term effects, where even for short durations of ice removal (~300 years), the removal of 1 km of ice results in an increased cumulative erupted mass long after the ice load is completely gone, are the most consequential in terms of the broader climate implications. Essentially, even if modern anthropogenic warming were curtailed immediately, the unloading that WARS subglacial volcanoes already experienced will still affect their behavior for hundreds to thousands of years to follow.

Given these unloading effects on the total mass erupted, we observe a stronger sensitivity of magma chambers that are initially saturated (i.e., Figures 6b–6d) subject to unloading compared to that of magma chambers that are initially volatile-undersaturated (compare with Figure S7 in Supporting Information S1). While the magma chamber is volatile-saturated and thus more compressible, a larger amount of mass must be evacuated in a single eruption to restore the magma chamber pressure to lithostatic (consider the effect of these larger eruptions compounded over the entirety of the eruptible lifetime of an initially volatile-saturated magma chamber, as compared to that for a magma chamber that only becomes saturated later in its evolution).

4.2. Addition to Enthalpy Budget

An increase in mass erupted from a subglacial magma chamber means more heat is introduced near the ice sheet. The enthalpy of an eruption is calculated as the sum of the sensible heat from the erupted material, Q_{sensible}, and the latent heat of crystallization and volatile exsolution, $Q_{\text{Latent},x}$ and $Q_{\text{Latent},e}$ respectively:

$$H_{\text{erupt}} = Q_{\text{sensible}} + Q_{\text{Latent},x} + Q_{\text{Latent},e}, \tag{14}$$

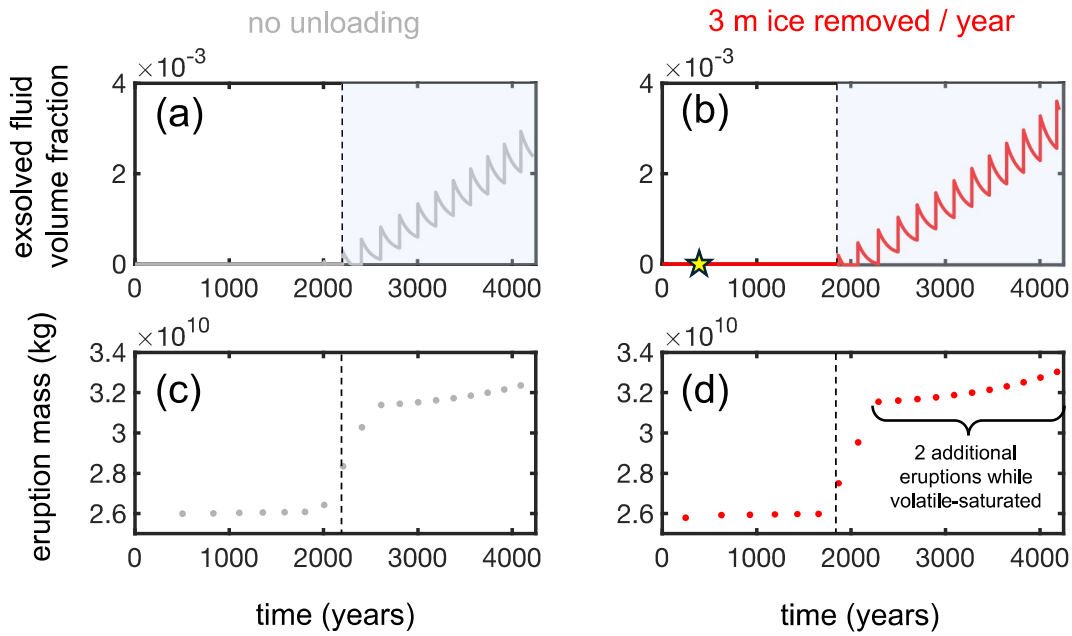


Figure 7. Eruptions Before and After Volatile Exsolution. Revisiting the magma chamber evolution from Figure 5, where the onset of volatile exsolution is expedited by 150 years the highest unloading rate for the removal of 1-km ice (3 m/yr). At this rate, the ice load is completely removed by 300 years (indicated by yellow star). Eruptions that occur while H_2O and CO_2 are still dissolved in the melt are notably smaller than those post volatile exsolution because of the profound increase in magma compressibility with subtle increases in the exsolved fluid volume fraction. When the magma chamber is subjected to the fast-unloading scenario, it erupts two additional times while the chamber is volatile-saturated than the equivalent magma chamber without unloading.

where

$$Q_{\text{sensible}} = \rho c T_{\text{er}} V_{\text{erupt}}, \tag{15}$$

$$Q_{\text{Latent},x} = \rho_x \varepsilon_x V_{\text{erupt}} L_x, \tag{16}$$

and

$$Q_{\text{Latent},e} = \rho_g \varepsilon_g V_{\text{erupt}} L_e. \tag{17}$$

L_x and L_e are provided in Table 1. Here, T_{er}, ε_x, and ε_g are the temperature, volume fraction of crystals, and exsolved fluid volume fraction, respectively, inside the magma chamber at the midpoint of the eruption. Figure S8 in Supporting Information S1 presents a regime diagram showing how the total erupted enthalpy from magma chamber deviates from the zero-unloading scenario at various rates of unloading.

Unloading-triggered volcanism will transfer additional enthalpy directly to the ice sheet base and/or surface once the erupted material penetrates through the ice. We can consider a theoretical average additional heat supply to the ice due to the volcanic response to unloading over time as follows:

$$q = \frac{H_{\text{erupt}}^{\text{with unloading}} - H_{\text{erupt}}^{\text{without unloading}}}{\text{eruptible lifetime of magma chamber}} \tag{18}$$

where the eruptible lifetime of the magma chamber is the duration of time over which the magma remains below $\varepsilon_x = 0.5$. Figure 8 demonstrates this additional heat input to the ice sheet for many magma chambers with initial volatile contents of 1 wt. % H_2O and 5,000 ppm CO_2 (volatile-saturated throughout their entire evolution). While additional heat released over time due to unloading could result from either a larger

15252027, 2024, 12, Downloaded from https://agupubs.onlinelibrary.wiley.com/doi/10.1029/2024GC011743 by Rwth Aachen University Universitätsbibliothek- 021000, Wiley Online Library on [18/12/2024]. See the Terms and Conditions (https://onlinelibrary.wiley.com/terms-and-conditions) on Wiley Online Library for rules of use; OA articles are governed by the applicable Creative Commons License

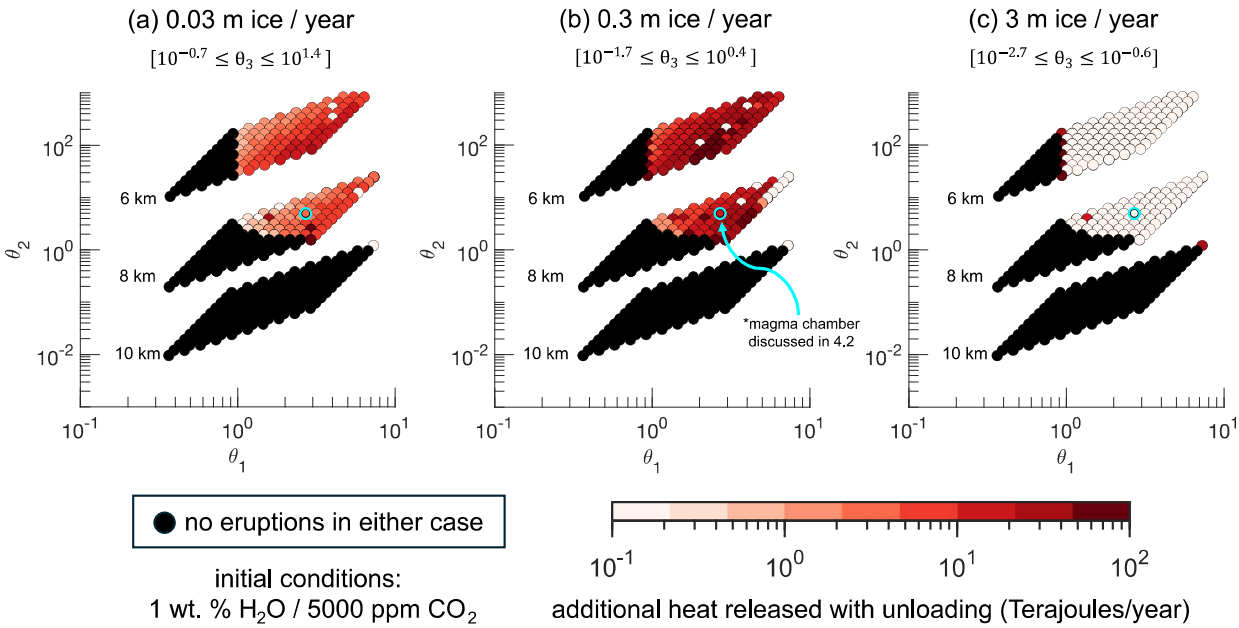


Figure 8. Regime diagram for magma chamber simulations at depths 6, 8, and 10 km in the crust, indicating the additional heat released in Terajoules per year due to unloading at various rates. All magma chambers have initial volatile contents of 1 wt. % H_2O and 5,000 ppm CO_2. Black circles represent magma chambers that do not exist in either case (with or without ice unloading). The magma chamber circled in cyan and indicated with an arrow is discussed further in the text.

erupted mass from the magma chamber without changes in its eruptible lifetime, or from the same (or less) erupted mass over a condensed eruptible lifetime, we find that unloading causes negligible changes in the eruptible lifetime of magma chambers that are initially volatile-saturated (see Figure S11 in Supporting Information S1). Hence, the sensitivity of magma chambers to this additional source of heat released over time in Figure 8 is primarily due to the increase in the total mass erupted with unloading. The highest rates of additional heat released due to unloading in Figure 8 are exhibited from magma chamber simulations subject to the intermediate unloading rate (0.3 m/yr). At even higher unloading rates, the 1-km ice load is removed rapidly with respect to the eruptible duration of the magma chamber simulation; once unloading "shuts off", the volumetric expansion-driven overpressure is gone. This means that only the unloading effects of greater magma compressibility and reduced pressure threshold for eruptions can increase the cumulative mass erupted in the longer term. At more moderate unloading rates, magma chambers subjected to the removal of a finite ice will experience the overpressure effect from volumetric expansion under decompression for a larger fraction of their eruptible lifetimes, which may compound the total heat released through eruptions over time. It is important to note that while modern ice loss rates may exceed those tested in this paper, modern subglacial magma chambers have also been experiencing a longer history of ice unloading, since the last glacial maximum (similar to the 30,000-year timescale for the removal of 1-km ice) and prior glacial cycles.

We consider the additional heat supplied from unloading-triggered volcanic effects on the magma chamber circled in cyan in Figure 8, which releases an additional 10 Terajoules per year at the intermediate unloading rate (0.3 m/yr). We calculate the amount of ice that can be melted by an additional 10 Terajoules (1×10^{12} J) per year to the ice sheet; the heat required to melt a mass, m, of ice is given by:

$$Q = m \cdot \Delta H_f \tag{19}$$

Taking the heat of fusion of water, ΔH_f, to be 334 J/g, the heat from unloading-triggered volcanism is capable of melting $\sim 3 \times 10^9$ kg of ice per year, or equivalently $\sim 3 \times 10^6$ m^3 of ice per year. This estimate stands for a single subglacial magma chamber at a depth of 8 km within the crust, with an initial volume of 1.5 km^3, subjected to the removal of 1-km ice at the intermediate unloading rate (0.3 m/yr).

15252027, 2024, 12, Downloaded from https://agupubs.onlinelibrary.wiley.com/doi/10.1029/2024GC011743 by Rwth Aachen University Universitätsbibliothek- 021000, Wiley Online Library on [18/12/2024]. See the Terms and Conditions (https://onlinelibrary.wiley.com/terms-and-conditions) on Wiley Online Library for rules of use; OA articles are governed by the applicable Creative Commons License

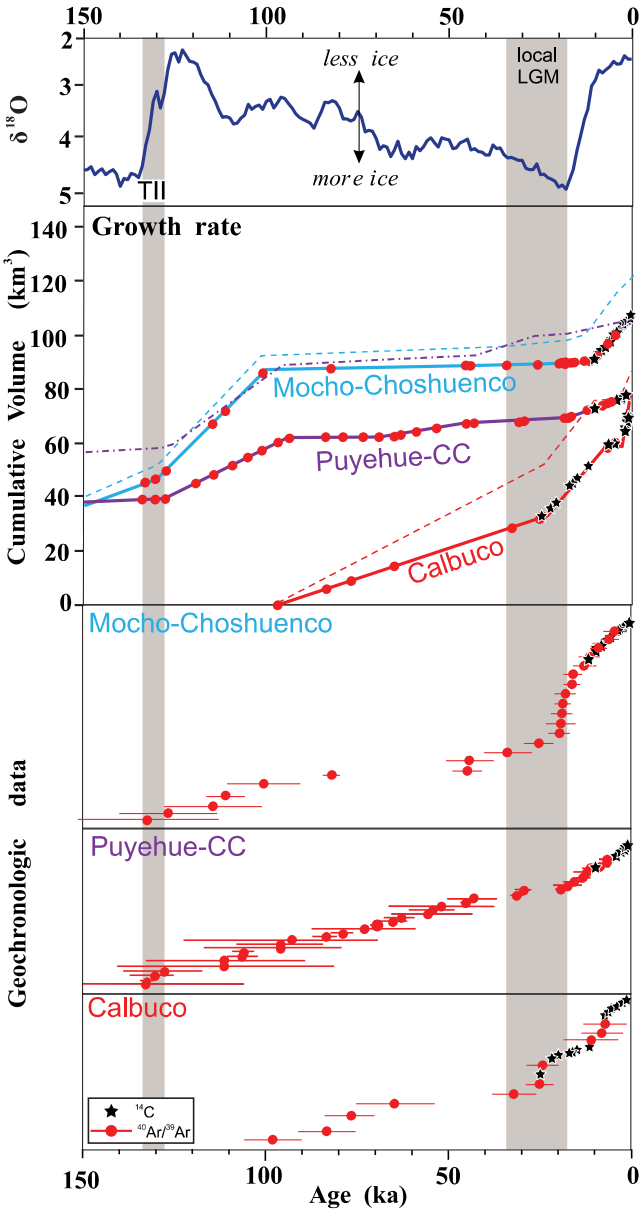


Figure 9. Records of cumulative volume erupted over time from three composite arc front volcanoes in the Andean Southern Volcanic Zone (Singer et al., 2024). $^{40}Ar/^{39}Ar$ ages from effusive lava flows and ^{14}C ages for tephra deposits have been used together with field relations to estimate eruptive volumes and growth rates (original data from Singer et al. (2008), Mixon et al. (2021), and Moreno-Yaeger et al. (2024)). Comparison with the global marine proxy record for global ice volume (Lisiecki & Raymo, 2005) indicates that following both Termination II (TII) and the local Last Glacial Maximum (LGM), cone growth rates markedly increase.

4.3. Supporting Evidence From the Geologic Record and Consequences for West Antarctica

While there is a timely need to understand the consequences of glacio-volcanic interactions for the assessment of risks both to local communities and globally as sea-level rises, it is difficult to probe recent subglacial volcanic activity (Iverson et al., 2017). Perhaps the most complete coupled records of volcanism and deglaciation are from the Southern Volcanic Zone of the Andes in South America, where the Patagonian ice sheet grew to its greatest thickness of 1,600 m or more atop several volcanic composite systems between about 35 and 18 ka, and retreated very rapidly between 18 and 15 ka (Mixon et al., 2021; Moreno-Yaeger et al., 2024; Rawson et al., 2016; Singer et al., 2024; Watt et al., 2013).

Figure 9 illustrates the increase in both cumulative volume erupted and the number of eruptions observed in the records from Calbuco, Mocho-Choshuenco, and Puyehue-Cordon Caulle volcanoes in the Andean arc following the local Last Glacial Maximum at 18 ka. These reconstructions that span the rapid, <3 Kyr, transition from glacial to post-glacial conditions suggest that there is a link between the rapid unloading of ice from the landscape and upticks in the frequency and volume of eruptions. As we have shown, magma chambers release more mass and heat with sufficiently high rates of ice unloading. Given that erupted volume is proportional to mass erupted, the records from these Andean volcanoes may be an illustration of the unloading-triggered behavior outlined in this study. Since the Andean records reflect arc magmas, which typically have higher initial volatile contents than rift magmas, they were likely volatile-saturated during the deglaciation. Our results suggest that volatile-saturated magma chambers are more sensitive to unloading-induced perturbations in erupted mass than magma chambers with a delayed onset of or without volatile exsolution, and hence the response of Andean volcanoes could be magnified in comparison to volcanoes in rift settings like West Antarctica. A positive feedback between unloading and magma chamber evolution could have accelerated deglaciation in the Andes from the heat released via eruptions and a decrease in ice albedo from subaerial volcanic deposits, potentially amplifying the volcanic response, in turn. While thick alpine glaciers remain atop some Andean volcanoes, they are typically narrow features (<1 km wide). Therefore, it is unlikely that the unloading of alpine ice can generate the requisite stress changes for eruptions at magma chamber depth (Singer et al., 2024). However, ice unloading in West Antarctica occurs over length scales more influential at depth, and thus increased volcanic activity may warrant consideration in the hazard assessment of future Antarctic expeditions.

Efforts that couple subglacial magmatic and/or volcanic evolution self-consistently with a variable pace of deglaciation (as in Singer et al. (2024)) can help provide evidence for the existence of an unstable feedback loop and inform the risk of runaway ice retreat in West Antarctica. Recalling from 4.2, the additional heat supplied from ice unloading effects on a particular magma chamber was $\sim 3 \times 10^9$ kg/yr; considering the more than 100 potentially active subglacial volcanoes of West Antarctica, the aggregate potential contribution to ice mass loss still pales in comparison, for example, to the estimated ~168 ± 78 Gt per year lost through the Amundsen Sea Embayment since 2010 (Davison et al., 2023) when considered in isolation. Even so, melted ice along the base of the ice sheet could facilitate sliding and ice loss to the ocean, and given the unloading effects on volcanism unaccounted for in our model at present (e.g., enhanced melt supply, stress conditions that promote dike initiation), this contribution to ice melting may be magnified. Nonetheless, this additional source of heat from the decreasing overburden pressure considered in this model contributes to uncertainty in the mass balance of the ice sheet and may play a

15252027, 2024, 12, Downloaded from https://agupubs.onlinelibrary.wiley.com/doi/10.1029/2024GC011743 by Rwth Aachen University Universitätsbibliothek - 021000, Wiley Online Library on [18/12/2024]. See the Terms and Conditions (https://onlinelibrary.wiley.com/terms-and-conditions) on Wiley Online Library for rules of use; OA articles are governed by the applicable Creative Commons License

15252027, 2024, 12, Downloaded from https://agupubs.onlinelibrary.wiley.com/doi/10.1029/2024GC011743 by Rwth Aachen University Universitätsbibliothek - 021000, Wiley Online Library on [18/12/2024]. See the Terms and Conditions (https://onlinelibrary.wiley.com/terms-and-conditions) on Wiley Online Library for rules of use; OA articles are governed by the applicable Creative Commons License

more important role in the ice sheet mass balance if there is in fact a positive feedback loop between deglaciation and volcanism. Given the precarious state of the West Antarctic Ice Sheet, this demonstration of additional heat input warrants consideration of glacio-volcanic feedbacks in projections of ice loss from West Antarctica.

5. Conclusions

We model the evolution of a subglacial magma chamber under various ice unloading rates to understand the physical mechanisms linking deglaciation and volcanism, with special consideration of the West Antarctic Rift System. To develop physical intuition for these processes, we consider ice unloading for a wide range of potential magma chambers. We find that a critical rate of unloading increases the total erupted mass from WARS-type (basaltic) subglacial magma chambers when simulating the removal of realistic ice loads (e.g., thickness on the km-scale). When the rate of ice unloading can compete with the rates of other processes affecting the internal dynamics of the magma chamber (i.e., magmatic recharge, cooling, and viscous relaxation of the surrounding crust), magma chambers produce additional eruptions due to the volumetric expansion of compressible magma inside the chamber, as well as a lowered critical pressure threshold required to trigger eruptions. In some cases, a longer duration of unloading at a more modest rate leads to more of these unloading-triggered eruptions than for short periods of extremely rapid unloading. Additionally, as the rate of unloading increases over magma chambers on the cusp of volatile saturation, the onset of the first exsolution of volatiles is expedited. Even after volatile saturation is reached, continued unloading increases the volume fraction of bubbles and hence, the compressibility of the magma. With increased magma compressibility, a larger amount of mass must be withdrawn during an eruption to relax the overpressure (Huppert & Woods, 2002; Townsend et al., 2019). Consequently, the total mass erupted from a magma chamber due to unloading is highly sensitive to the volume fraction of exsolved volatiles. Even long after ice unloading ceases, the compressibility of the magma remains permanently elevated due to the reduction in lithostatic pressure, resulting in larger eruptions compounding over the long-term trajectory of the magma chamber. The additional heat associated with such unloading-triggered eruptions is currently unaccounted for in models of the West Antarctic Ice Sheet, despite its potential to perturb the surface mass balance and/or basal sliding rate of an already critically vulnerable ice sheet. In the interest of elucidating hazards both in terms of fieldwork in West Antarctica and global sea-level rise, more work must be done to determine whether other glacio-volcanic feedbacks will amplify modern ice loss.

Conflict of Interest

The authors declare no conflicts of interest relevant to this study.

Data Availability Statement

The Matlab scripts to run this model are available in the following Zenodo repository: https://doi.org/10.5281/zenodo.12188625 (Coonin et al., 2024).

Acknowledgments
The paper was significantly improved thanks to comments from A. Geyer and M. Van Wyk de Vries. Supplementary Information is available for this paper. Correspondence and requests for materials should be addressed to Allie N. Coonin. This work was supported by NSF Grants EAR-2121655, EAR-2121570, and EAR-2444709.

References

Annen, C. (2009). From plutons to magma chambers: Thermal constraints on the accumulation of eruptible silicic magma in the upper crust. *Earth and Planetary Science Letters*, *284*(3–4), 409–416. https://doi.org/10.1016/j.epsl.2009.05.006

Aubry, T. J., Farquharson, J. I., Rowell, C. R., Watt, S. F. L., Pinel, V., Beckett, F., et al. (2022). Impact of climate change on volcanic processes: Current understanding and future challenges. *Bulletin of Volcanology*, *84*(6), 58. https://doi.org/10.1007/s00445-022-01562-8

Barletta, V. R., Bevis, M., Smith, B. E., Wilson, T., Brown, A., Bordoni, A., et al. (2018). Observed rapid bedrock uplift in Amundsen Sea Embayment promotes ice-sheet stability. *Science*, *360*(6395), 1335–1339. https://doi.org/10.1126/science.aao1447

Behrendt, J. C., Blankenship, D. D., Morse, D. L., Finn, C. A., & Bell, R. E. (2002). Subglacial volcanic features beneath the West Antarctic Ice Sheet interpreted from aeromagnetic and radar ice sounding. *Geological Society, London, Special Publications*, *202*(1), 337–355. https://doi.org/10.1144/GSL.SP.2002.202.01.1

Blankenship, D. D., Bell, R. E., Hodge, S. M., Brozena, J. M., Behrendt, J. C., & Finn, C. A. (1993). Active volcanism beneath the West Antarctic ice sheet and implications for ice-sheet stability. *Nature*, *361*(6412), 526–529. https://doi.org/10.1038/361526A0

Bray, J. R. (1979). Surface albedo increase following massive Pleistocene explosive eruptions in western North America. *Quaternary Research*, *12*(2), 204–211. https://doi.org/10.1016/0033-5894(79)90057-7

Caricchi, L., Burlini, L., Ulmer, P., Gerya, T., Vassalli, M., & Papale, P. (2007). Non-Newtonian rheology of crystal-bearing magmas and implications for magma ascent dynamics. *Earth and Planetary Science Letters*, *264*(3–4), 402–419. https://doi.org/10.1016/j.epsl.2007.09.032

Chen, J. L., Wilson, C. R., Blankenship, D. D., & Tapley, B. D. (2006). Antarctic mass rates from GRACE. *Geophysical Research Letters*, *33*(11), L11502. https://doi.org/10.1029/2006GL026369

Coonin, A. N., Huber, C., Townsend, M., Troch, J., & Scholz, K. (2024). *Subglacial magma chamber model with ice unloading* [Software]. Zenodo. https://doi.org/10.5281/zenodo.12188625

Corr, H., & Vaughan, D. (2008). A recent volcanic eruption beneath the West Antarctic ice sheet. *Nature Geoscience*, *1*(2), 122–125. https://doi.org/10.1038/ngeo106

Davison, B. J., Hogg, A. E., Rigby, R., Veldhuijsen, S., van Wessem, J. M., van den Broeke, M. R., et al. (2023). Sea level rise from West Antarctic mass loss significantly modified by large snowfall anomalies. *Nature Communications*, *14*(1), 1479. https://doi.org/10.1038/s41467-023-36990-3

Degruyter, W., & Huber, C. (2014). A model for eruption frequency of upper crustal silicic magma chambers. *Earth and Planetary Science Letters*, *403*, 117–130. https://doi.org/10.1016/j.epsl.2014.06.047

Degruyter, W., Huber, C., Bachmann, O., Cooper, K. M., & Kent, A. J. (2017). Influence of exsolved volatiles on reheating silicic magmas by recharge and consequences for eruptive style at Volcán Quizapu (Chile). *Geochemistry, Geophysics, Geosystems*, *18*(11), 4123–4135. https://doi.org/10.1002/2017gc007219

DIGIS Team. (2023). "2023-12-KAIVCT_ANTARCTICA.csv", GEOROC compilation: Rift volcanics [Dataset]. *GRO.data, V9*. https://doi.org/10.25625/KAIVCT/NSXCRD

ETNA, Bulletin Settimanale 26/07/2021-01/08/2021, Rep. N 31/2021. (2021). INGV.

Fretwell, P., Pritchard, H. D., Vaughan, D. G., Bamber, J. L., Barrand, N. E., Bell, R., et al. (2013). Bedmap2: Improved ice bed, surface and thickness datasets for Antarctica. *The Cryosphere*, *7*(1), 375–393. https://doi.org/10.5194/tc-7-375-2013

Gelman, S. E., Gutiérrez, F. J., & Bachmann, O. (2013). On the longevity of large upper crustal silicic magma reservoirs. *Geology*, *41*(7), 759–762. https://doi.org/10.1130/g34241.1

Geyer, A., Di Roberto, A., Smellie, J., Van Wyk de Vries, M., Panter, K., Martin, A., et al. (2023). Volcanism in Antarctica: An assessment of the present state of research and future directions. *Journal of Volcanology and Geothermal Research*, *444*(2023), 107941. https://doi.org/10.1016/j.jvolgeores.2023.107941

Ghiorso, M. S., & Gualda, G. A. R. (2015). An H_2O–CO_2 mixed fluid saturation model compatible with rhyolite-MELTS. *Contributions to Mineralogy and Petrology*, *169*(6), 53. https://doi.org/10.1007/s00410-015-1141-8

Gomez, N., Pollard, D., & Holland, D. (2015). Sea-level feedback lowers projections of future Antarctic Ice-Sheet mass loss. *Nature Communications*, *6*(1), 8798. https://doi.org/10.1038/ncomms9798

Gomez, N., Weber, M. E., Clark, P. U., Mitrovica, J. X., & Han, H. K. (2020). Antarctic ice dynamics amplified by Northern Hemisphere sea-level forcing. *Nature*, *587*(7835), 600–604. https://doi.org/10.1038/s41586-020-2916-2

Gualda, G. A., Ghiorso, M. S., Lemons, R. V., & Carley, T. L. (2012). Rhyolite-MELTS: A modified calibration of MELTS optimized for silica-rich, fluid-bearing magmatic systems. *Journal of Petrology*, *53*(5), 875–890. https://doi.org/10.1093/petrology/egr080

Handler, P. (1989). The effect of volcanic aerosols on global climate. *Journal of Volcanology and Geothermal Research*, *37*(3–4), 233–249. https://doi.org/10.1016/0377-0273(89)90081-4

Hogg, A. E., Gilbert, L., Shepherd, A., Muir, A. S., & McMillan, M. (2021). Extending the record of Antarctic ice shelf thickness change, from 1992 to 2017. *Advances in Space Research*, *68*(2), 724–731. https://doi.org/10.1016/j.asr.2020.05.030

Huber, C., Bachmann, O., & Manga, M. (2009). Homogenization processes in silicic magma chambers by stirring and mushification (latent heat buffering). *Earth and Planetary Science Letters*, *283*(1–4), 38–47. https://doi.org/10.1016/j.epsl.2009.03.029

Huppert, H., & Woods, A. (2002). The role of volatiles in magma chamber dynamics. *Nature*, *420*(6915), 493–495. https://doi.org/10.1038/nature01211

Huybers, K., Roe, G., & Conway, H. (2017). Basal topographic controls on the stability of the West Antarctic ice sheet: Lessons from Foundation Ice Stream. *Annals of Glaciology*, *58*(75pt2), 193–198. https://doi.org/10.1017/aog.2017.9

Huybers, P., & Langmuir, C. (2009). Feedback between deglaciation, volcanism, and atmospheric CO_2. *Earth and Planetary Science Letters*, *286*(3–4), 479–491. https://doi.org/10.1016/j.epsl.2009.07.014

Iverson, N. A., Lieb-Lappen, R., Dunbar, N. W., Obbard, R., Kim, E., & Golden, E. (2017). The first physical evidence of subglacial volcanism under the West Antarctic Ice Sheet. *Scientific Reports*, *7*(1), 11457. https://doi.org/10.1038/s41598-017-11515-3

Jellinek, A. M., & DePaolo, D. J. (2003). A model for the origin of large silicic magma chambers: Precursors of caldera-forming eruptions. *Bulletin of Volcanology*, *65*(5), 363–381. https://doi.org/10.1007/s00445-003-0277-y

Jellinek, A. M., Manga, M., & Saar, M. O. (2004). Did melting glaciers cause volcanic eruptions in eastern California? Probing the mechanics of dike formation. *Journal of Geophysical Research*, *109*(B9), B09206. https://doi.org/10.1029/2004jb002978

Jull, M., & McKenzie, D. (1996). The effect of deglaciation on mantle melting beneath Iceland. *Journal of Geophysical Research*, *101*(B10), 21815–21828. https://doi.org/10.1029/96JB01308

LeMasurier, W. (2013). Shield volcanoes of Marie Byrd Land, West Antarctic rift: Oceanic island similarities, continental signature, and tectonic controls. *Bulletin of Volcanology*, *75*(6), 726. https://doi.org/10.1007/s00445-013-0726-1

LeMasurier, W. E., Thomson, J. W., Baker, P. E., Kyle, P. R., Rowley, P. D., Smellie, J. L., & Verwoerd, W. J. (1990). *Volcanoes of the Antarctic plate and southern ocean* (Vol. 48). American Geophysical Union. Antarctic Research Series. https://doi.org/10.1029/AR048

Lisiecki, L. E., & Raymo, M. E. (2005). A Pliocene-Pleistocene stack of 57 globally distributed benthic $\delta^{18}O$ records. *Paleoceanography*, *20*(1). https://doi.org/10.1029/2004pa001071

Liu, Y., Zhang, Y., & Behrens, H. (2005). Solubility of H_2O in rhyolitic melts at low pressures and a new empirical model for mixed H_2O–CO_2 solubility in rhyolitic melts. *Journal of Volcanology and Geothermal Research*, *143*(1–3), 219–235. https://doi.org/10.1016/j.jvolgeores.2004.09.019

Lough, A. C., Wiens, D. A., Grace Barcheck, C., Anandakrishnan, S., Aster, R. C., Blankenship, D. D., et al. (2013). Seismic detection of an active subglacial magmatic complex in Marie Byrd Land, Antarctica. *Nature Geoscience*, *6*(12), 1031–1035. https://doi.org/10.1038/ngeo1992

Lowenstern, J. B. (2001). Carbon dioxide in magmas and implications for hydrothermal systems. *Mineralium Deposita*, *36*(6), 490–502. https://doi.org/10.1007/s001260100185

Maclennan, J., Jull, M., McKenzie, D., Slater, L., & Grönvold, K. (2002). The link between volcanism and deglaciation in Iceland. *Geochemistry, Geophysics, Geosystems*, *3*(11), 1–25. https://doi.org/10.1029/2001GC000282

Marsh, B. D. (1981). On the crystallinity, probability of occurrence, and rheology of lava and magma. *Contributions to Mineralogy and Petrology*, *78*(1), 85–98. https://doi.org/10.1007/bf00371146

Mason, B. G., Pyle, D. M., & Oppenheimer, C. (2004). The size and frequency of the largest explosive eruptions on Earth. *Bulletin of Volcanology*, *66*(8), 735–748. https://doi.org/10.1007/s00445-004-0355-9

Mixon, E. E., Singer, B. S., Jicha, B. R., & Ramirez, A. (2021). Calbuco, a monotonous andesitic high-flux volcano in the Southern Andes, Chile. *Journal of Volcanology and Geothermal Research*, *416*, 107279. https://doi.org/10.1016/j.jvolgeores.2021.107279

Möller, R., Dagsson-Waldhauserova, P., Möller, M., Kukla, P. A., Schneider, C., & Gudmundsson, M. T. (2019). Persistent albedo reduction on southern Icelandic glaciers due to ashfall from the 2010 Eyjafjallajökull eruption. *Remote Sensing of Environment*, *233*, 111396. https://doi.org/10.1016/j.rse.2019.111396

15252027, 2024, 12, Downloaded from https://agupubs.onlinelibrary.wiley.com/doi/10.1029/2024GC011743 by Rwth Aachen University Universitätsbibliothek - 021000, Wiley Online Library on [18/12/2024]. See the Terms and Conditions (https://onlinelibrary.wiley.com/terms-and-conditions) on Wiley Online Library for rules of use; OA articles are governed by the applicable Creative Commons License

Mora, D., & Tassara, A. (2019). Upper crustal decompression due to deglaciation-induced flexural unbending and its role on post-glacial volcanism at the Southern Andes. *Geophysical Journal International*, *216*(3), 1549–1559. https://doi.org/10.1093/gji/ggy473

Moreno-Yaeger, P., Singer, B. S., Edwards, B. R., Jicha, B. R., Nachlas, W. O., Kurz, M. D., et al. (2024). Pleistocene to recent evolution of Mocho-Choshuenco volcano during growth and retreat of the Patagonian Ice Sheet. *Geological Society of America Bulletin*, *136*(11–12), 5262–5282. https://doi.org/10.1130/B37514.1

Moussallam, Y., Oppenheimer, C., Scaillet, B., Gaillard, F., Kyle, P., Peters, N., et al. (2014). Tracking the changing oxidation state of Erebus magmas, from mantle to surface, driven by magma ascent and degassing. *Earth and Planetary Science Letters*, *393*, 200–209. https://doi.org/10.1016/j.epsl.2014.02.055

Oppenheimer, C., Scaillet, B., & Martin, R. S. (2011). Sulfur degassing from volcanoes: Source conditions, surveillance, plume chemistry and earth system impacts. *Reviews in Mineralogy and Geochemistry*, *73*(1), 363–421. https://doi.org/10.2138/rmg.2011.73.13

Pegler, S. S. (2018). Marine ice sheet dynamics: The impacts of ice-shelf buttressing. *Journal of Fluid Mechanics*, *857*, 605–647. https://doi.org/10.1017/jfm.2018.741

Rawson, H., Pyle, D. M., Mather, T. A., Smith, V. C., Fontijn, K., Lachowycz, S. M., & Naranjo, J. A. (2016). The magmatic and eruptive response of arc volcanoes to deglaciation: Insights from southern Chile. *Geology*, *44*(4), 251–254. https://doi.org/10.1130/G37504.1

Rubin, A. M. (1995). Propagation of magma-filled cracks. *Annual Review of Earth and Planetary Sciences*, *23*(23), 287–336. https://doi.org/10.1146/annurev.earth.23.1.287

Satow, C., Gudmundsson, A., Gertisser, R., Ramsey, C. B., Bazargan, M., Pyle, D. M., et al. (2021). Eruptive activity of the Santorini Volcano controlled by sea-level rise and fall. *Nature Geoscience*, *14*(8), 586–592. https://doi.org/10.1038/s41561-021-00783-4

Scholz, K., Townsend, M., Huber, C., Troch, J., Bachmann, O., & Coonin, A. N. (2023). Investigating the impact of an exsolved H_2O-CO_2 phase on magma chamber growth and longevity: A thermomechanical model. *Geochemistry, Geophysics, Geosystems*, *24*(12), e2023GC011151. https://doi.org/10.1029/2023GC011151

Schroeder, D. M., Blankenship, D. D., Young, D. A., & Quartini, E. (2014). Evidence for elevated and spatially variable geothermal flux beneath the West Antarctic Ice Sheet. *Proceedings of the National Academy of Sciences of the United States of America*, *111*(25), 9070–9072. https://doi.org/10.1073/pnas.1405184111

Shapiro, N. M., & Ritzwoller, M. H. (2004). Inferring surface heat flux distributions guided by a global seismic model: Particular application to Antarctica. *Earth and Planetary Science Letters*, *223*(1–2), 213–224. https://doi.org/10.1016/j.epsl.2004.04.011

Sigmundsson, F., Pinel, V., Lund, B., Albino, F., Pagli, C., Geirsson, H., & Sturkell, E. (2010). Climate effects on volcanism: Influence on magmatic systems of loading and unloading from ice mass variations, with examples from Iceland. *Philosophical Transactions of the Royal Society A: Mathematical, Physical & Engineering Sciences*, *368*(1919), 2519–2534. https://doi.org/10.1098/rsta.2010.0042

Singer, B. S., Jicha, B. R., Naranjo, J. A., Lara, L. E., Moreno-Roa, H., & Harper, M. A. (2008). Eruptive history, geochronology, and magmatic evolution of the Puyehue-Cordon Caulle volcanic complex, Chile. *Geological Society of America Bulletin*, *120*(5–6), 599–618. https://doi.org/10.1130/b26276.1

Singer, B. S., Moreno-Yaeger, P., Townsend, M., Huber, C., Cuzzone, J., Edwards, B. R., et al. (2024). New perspectives on ice forcing in continental arc magma plumbing systems. *Journal of Volcanology and Geothermal Research*, *455*, 108187. https://doi.org/10.1016/j.jvolgeores.2024.108187

Smellie, J. L., & Edwards, B. R. (2016). *Glaciovolcanism on Earth and Mars*. Cambridge University Press.

Spiegel, C., Lindow, J., Kamp, P. J., Meisel, O., Mukasa, S., Lisker, F., et al. (2016). Tectonomorphic evolution of Marie Byrd Land—Implications for Cenozoic rifting activity and onset of West Antarctic glaciation. *Global and Planetary Change*, *145*(2016), 98–115. https://doi.org/10.1016/j.gloplacha.2016.08.013

Stevens, C., Hulbe, C., Brewer, M., Stewart, C., Robinson, N., Ohneiser, C., & Jendersie, S. (2020). Ocean mixing and heat transport processes observed under the ross ice shelf control its basal melting. *Proceedings of the National Academy of Sciences of the United States of America*, *117*(29), 16799–16804. https://doi.org/10.1073/pnas.1910760117

Sutter, J., Jones, A., Frölicher, T. L., Wirths, C., & Stocker, T. F. (2023). Climate intervention on a high-emissions pathway could delay but not prevent West Antarctic Ice Sheet demise. *Nature Climate Change*, *13*(9), 951–960. https://doi.org/10.1038/s41558-023-01738-w

Taisne, B., Tait, S., & Jaupart, C. (2011). Conditions for the arrest of a vertical propagating dyke. *Bulletin of Volcanology*, *73*(2), 191–204. https://doi.org/10.1007/s00445-010-0440-1

Townsend, M., & Huber, C. (2020). A critical magma chamber size for volcanic eruptions. *Geology*, *48*(5), 431–435. https://doi.org/10.1130/g47045.1

Townsend, M., Huber, C., Degruyter, W., & Bachmann, O. (2019). Magma chamber growth during intercaldera periods: Insights from thermo-mechanical modeling with applications to Laguna del Maule, Campi Flegrei, Santorini, and Aso. *Geochemistry, Geophysics, Geosystems*, *20*(3), 1574–1591. https://doi.org/10.1029/2018gc008103

Van Wyk de Vries, M., Bingham, R. G., & Hein, A. S. (2018). A new volcanic province: An inventory of subglacial volcanoes in West Antarctica. *Geological Society, London, Special Publications*, *461*(1), 231–248. https://doi.org/10.1144/SP461.7

Watt, S. F., Pyle, D. M., & Mather, T. A. (2013). The volcanic response to deglaciation: Evidence from glaciated arcs and a reassessment of global eruption records. *Earth-Science Reviews*, *122*, 77–102. https://doi.org/10.1016/j.earscirev.2013.03.007

Wilson, A. M., & Russell, J. K. (2020). Glacial pumping of a magma-charged lithosphere: A model for glaciovolcanic causality in magmatic arcs. *Earth and Planetary Science Letters*, *548*, 116500. https://doi.org/10.1016/j.epsl.2020.116500

References From the Supporting Information

Giordano, G., Lucci, F., Phillips, D., Cozzupoli, D., & Runci, V. (2012). Stratigraphy, geochronology and evolution of the Mt. Melbourne volcanic field (North Victoria Land, Antarctica). *Bulletin of Volcanology*, *74*, 1985–2005. https://doi.org/10.1007/s00445-012-0643-8

Kim, J., Park, J. W., Lee, M. J., Lee, J. I., & Kyle, P. R. (2019). Evolution of alkalic magma systems: insight from coeval evolution of sodic and potassic fractionation lineages at the Pleiades volcanic complex, Antarctica. *Journal of Petrology*, *60*(1), 117–150. https://doi.org/10.1093/petrology/egy108

LeMasurier, W. E., Choi, S. H., Kawachi, Y., Mukasa, S. B., & Rogers, N. W. (2011). Evolution of pantellerite-trachyte-phonolite volcanoes by fractional crystallization of basanite magma in a continental rift setting, Marie Byrd Land, Antarctica. *Contributions to Mineralogy and Petrology*, *162*, 1175–1199. https://doi.org/10.1007/s00410-011-0646-z

Licht, K. J., Groth, T., Townsend, J. P., Hennessy, A. J., Hemming, S. R., Flood, T. P., & Studinger, M. (2018). Evidence for extending anomalous Miocene volcanism at the edge of the East Antarctic craton. *Geophysical Research Letters*, *45*(7), 3009–3016. https://doi.org/10.1002/2018GL077237

15252027, 2024, 12, Downloaded from https://agupubs.onlinelibrary.wiley.com/doi/10.1029/2024GC011743 by Rwth Aachen University Universitätsbibliothek - 021000, Wiley Online Library on [18/12/2024]. See the Terms and Conditions (https://onlinelibrary.wiley.com/terms-and-conditions) on Wiley Online Library for rules of use; OA articles are governed by the applicable Creative Commons License

Rocchi, S., Armienti, P., D'Orazio, M., Tonarini, S., Wijbrans, J. R., & Di Vincenzo, G. (2002). Cenozoic magmatism in the western Ross Embayment: Role of mantle plume versus plate dynamics in the development of the West Antarctic Rift System. *Journal of Geophysical Research*, *107*(B9), ECV-5-1–ECV 5-22. https://doi.org/10.1029/2001JB000515

15252027, 2024, 12, Downloaded from https://agupubs.onlinelibrary.wiley.com/doi/10.1029/2024GC011743 by Rwth Aachen University Universitätsbibliothek- 021000, Wiley Online Library on [18/12/2024]. See the Terms and Conditions (https://onlinelibrary.wiley.com/terms-and-conditions) on Wiley Online Library for rules of use; OA articles are governed by the applicable Creative Commons License